Alma Mater Studiorum · Università di Bologna

Scuola di Scienze
Dipartimento di Fisica e Astronomia
Corso di Laurea Magistrale in Fisica

Towards an improved Photonic Force Microscope: a novel technique for biological microscopy

Relatore:
Prof. Gastone Castellani

Presentata da:
Eliana Battistella

Correlatori:
Dott. Francesco Pedaci
Dott.ssa Zhanna Santybayeva

Anno Accademico 2016/2017

Abstract

Questo lavoro di tesi è stato svolto nel gruppo di *Single-molecule angular dynamics* del dott. Pedaci, presso il *Centre de Biochimie Structurale* di Montpellier, laboratorio del *Centre National de la Recherche Scientifique*.

Il lavoro si inserisce all'interno dell'ambito di ricerca in biofisica e nello sviluppo di nuove tecniche in microscopia, al fine dello studio topografico di campioni biologici.

Una delle tecniche più conosciute e utilizzate è l'*Atomic Force Microscope*, che consente di ottenere immagini accurate e ad alta risoluzione. Questo metodo però ha delle limitazioni dovute alla presenza di un *cantilever* meccanico. Questo pone un limite nella forza minima applicabile su un campione per ottenere un'immagine topografica. Questa forza minima è dell'ordine delle decine dei piconewton e può essere sufficiente a danneggiare il campione e a deformare i dettagli topografici che invece si vorrebbero evidenziare.

Per superare questa problematica si può utilizzare un *Photonic Force Microscope*, dove il *cantilever* è sostituito dalle *optical tweezers*. Questa tecnica permette di effettuare scansioni di campioni biologici applicando forze dell'ordine delle centinaia di femtonewton. All'interno della trappola ottica viene posizionata una microparticella che agisce da sonda, attraverso la quale possono essere rilevati i dettagli topografici del campione.

La differenza rispetto al *Photonic Force Microscope* tradizionale si trova proprio nel tipo di sonda utilizzata durante la scansione. Lo standard prevede l'utilizzo di una microparticella sferica, di dimensioni dell'ordine delle centinaia di nanometri mentre l'ipotesi è che si possano utilizzare delle sonde cilindriche con alla base un dettaglio acuminato che richiama la punta dell'AFM. Questo tipo di sonda consentirebbe di raggiungere una risoluzione maggiore, rispetto al PFM tradizionale, che risente del limite dato dal diametro della sfera.

Due differenti setup per la PFM sono stati costruiti e testati durante questo periodo di tesi. Sono state testate diverse microparticelle cilindriche, di dimensioni differenti in termini di *aspect ratio* con lo scopo di osservare la stabilità di questo tipo di sonda. Nei risultati viene proposto un metodo per controllare la stabilità e l'orientazione della microparticella cilindrica all'interno della trappola ottica. Viene inoltre fatta un'ipotesi su un metodo per stimare la lunghezza della punta che dovrà essere verificata da una misura sistematica. Infine i risultati preliminari riguardanti la scansione di strutture note sembrano suggerire la validità dell'uso di questo nuovo tipo di sonda.

Contents

Overview

This thesis project has been developed in the Centre de Biochimie Structurale in Montpellier, France, in the Single-Molecule Angular Dynamics group of F. Pedaci, under a direct supervision of Z. Santybayeva, and in a collaboration with R. Desgarceaux and B. Charlot from the Institut d'Electronique et des systèmes, Montpellier.

Scanning Probe Microscopy techniques have proven to be valuable in the studies about the physical properties like viscoelasticity, rigidity, dynamics, and structure of many biological and non-biological systems. One of the more known and well established of them is the Atomic Force Microscopy technique, which permits to obtain accurate measurements of the interaction forces, the rigidity, and the high-resolution topography of polymers, protein complexes, cell membranes, etc. Even so, the AFM has a limitation in applications where ultra-soft samples are analyzed. The typical forces required for stable imaging (piconewtons) can lead to partial damage of the sample.

In this work, an alternative technique, the Photonic Force Microscopy was used because it can overcome the limitation of the AFM by substituting the mechanical cantilever by a weak optical trap. The use of an optical trap permits imaging of soft substrates with sub-piconewton forces. Moreover, the standard spherical probe was replaced with cylindrical probes with narrow protrusions on the top in order to improve the axial resolution. The system was complemented with the specially designed Graphical user interface for data analysis and topographical image reconstruction.

The thesis has a following structure.

Chapter 1 gives an overview on the optical tweezers technique. In particular, the physical principles and the applications are introduced, with a particular emphasis on the Photonic Force Microscope technique. The following Chapter 2 provides a detailed description of the two different setups, together with the optics alignment method. Then, the methods used to calibrate the optical trap and the development of a dedicated software are explained. The variety of probes and samples studied are described. Lastly, the image acquisition process and the data analysis that brings to the image reconstruction are illustrated. Chapter 3 shows the results of the double-beam PFM and of the single-beam PFM. A method to assess the orientation of the probe in the optical trap (tip up or down) in terms of intensity level of the axial signal is proposed. Moreover, a single preliminary measurement to estimate the length of the tip is presented. Finally, in Chapter 4 the experimental outcomes are discussed, and the final conclusions and perspectives are presented in Chapter 5.

Introduction to Optical Tweezers

1.1 Optical tweezers

The field of laser-based optical trapping started to develop following the research of Arthur Ashkin, which first demonstrated that the forces of radiation pressure can accelerate freely suspended particles [1]. Even before the advent of lasers, it was known that light can exert radiation pressure on objects [2]. However, the resulting forces due to the presence of radiometric effects are usually orders of magnitude larger than radiation pressure. Therefore these effects were hardly detectable because of their minuteness and the study of this subject was considered not applicable to practical cases. Later, with the much higher intensities producible by lasers it became possible to study optical forces. It is Ashkin's idea of using dielectric particles suspended in transparent media that has allowed quantitative observation of the tiny radiation pressure [1].
Back then, in the early 1970s, Ashkin observed that micron-sized particles can experience an acceleration due to radiation forces, whose direction is bound to the index of refraction of the particle with respect to that of the suspension medium [1]. After this discovery, in 1986 Ashkin showed that these particles can be trapped in an optical potential well using only the force of radiation pressure from a continuous laser with a Gaussian profile [3]. This trapping is stable in three dimensions and is characterised by an equilibrium point: any displacement of the trapped particle away from the point of equilibrium results in a restoring force, which brings the particle back.
From that moment on, the research in the field experienced a great development and this technique has been employed to trap and manipulate different types of micro-particles, atoms and molecules as well as living biological cells and organelles within cells [4]–[6]. For instance, the development of optical cooling and trapping has led to the first observation of Bose-Einstein condensation of atomic vapours in single-atom traps [7]. Furthermore, the unique characteristics of these manipulation techniques, often called optical tweezers (OT), have impacted various subfields of physics, chemistry and biology. As far as biological sciences and chemistry are concerned, the possibility to measure and control optical forces having the magnitude between hundredths of a piconewton and hundreds of piconewtons has led to studies of mechanical forces and viscoelastic properties of cells and molecules while avoiding sample damage [8]. Moreover, as it will be discussed further, optical trapping has favoured the studies of mechanics, force generation

and kinetics of cellular motor proteins and mechanoenzymes [9]–[11].

Finally, to understand the basic principles of optical trapping only concepts of momentum conservation and ray optics theory are needed, although a full theory for optical tweezers has not been developed yet. In fact, such factors as size, shape, material and dimensions of trapped objects with respect to the wavelength of the laser light influence the response of the trap, therefore, to develop a more complete theory it is necessary to consider many elements requiring a vectorial treatment, which is not straightforward.

In the next sections different types of optical tweezers and some of their applications will be described.

1.1.1 Types

There are many possible configuration of optical traps. Some of them will be briefly described in the following paragraphs.

Counter propagating beams

This configuration was the first true optical potential well [1]. It was constructed using two equal TEM_{00} Gaussian beams propagating in the opposite directions as shown in figure 1.1. The equilibrium point for a sphere with a high index of refraction is at the symmetry point between the two beams. In fact, the interruption of one beam causes acceleration of the sphere along the direction of propagation of the remaining beam and when the first beam is turned on again the particle returns to the equilibrium point.

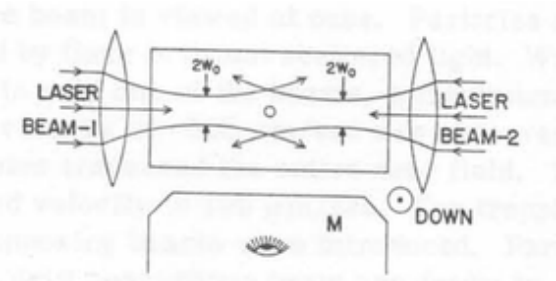

Figure 1.1: Geometry of the first optical trap obtained using two counterpropagating laser beams [1].

Optical levitation

Another possible configuration uses a single laser beam to levitate stably a dielectric sphere in air or in vacuum [12]. To achieve this, a single TEM_{00} Gaussian beam is focused vertically creating an optical well with an equilibrium point achieved when radiation pressure and gravity counterbalance. In figure 1.2 the configuration used by Ashkin in his optical levitation experiment [12] is shown.

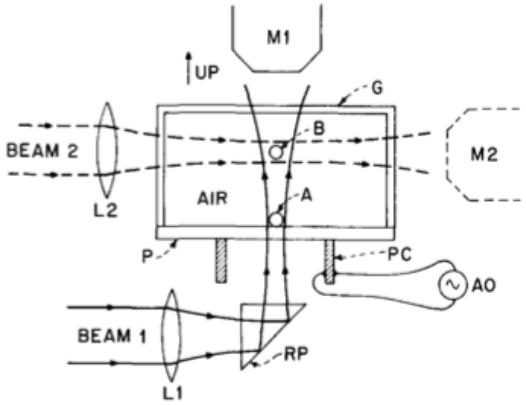

Figure 1.2: Geometry of the optical levitation apparatus, radiation pressure from laser beam 1 is counterbalanced by gravity whereas beam 2 has been introduced only to study the strength of the trapping forces [12].

Single beam

In 1986, Ashkin demonstrated for the first time the possibility of stable trapping of dielectric spheres using a single strongly focused beam [3]. Here, particles with sizes in a wide range can be trapped stably (from 10 μm down to 25 nm) in aqueous media making this configuration especially interesting. The forces acting on a trapped sphere will be treated in detail in the next section.

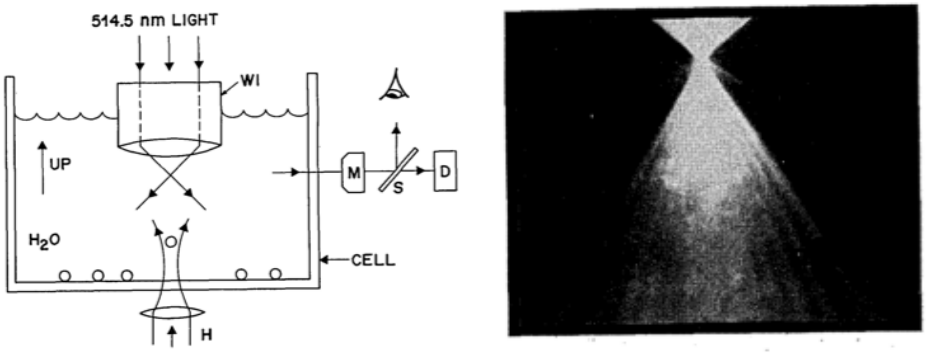

(a) (b)

Figure 1.3: (a) Sketch of the apparatus used by Ashkin to obtain an optical trap using a single beam. (b) Photograph of a 10 μm bead trapped in water [3].

Holographic trap

Holographic optical tweezers use computer generated holograms called *diffractive optical elements* to split a single laser beam in N-simultaneous optical traps [13]–[15]. Each of these traps can be defined with their proper characteristics such as stiffness, and the entire pattern can be updated by dynamically transforming the

initial layout. Thanks to the possibility to project hundreds of optical traps simultaneously in an arbitrary 3D configuration this technique is applied in numerous areas such as biomedical testing and diagnostics, photonics manufacturing, biological and chemical sensor fabrication, and assembly of hierarchically structured functional nanocomposite materials [16]–[18].

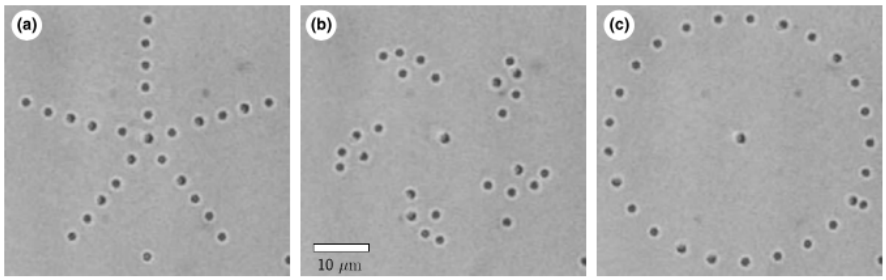

Figure 1.4: Transformation of trapping configuration of silica spheres using dynamic holographic optical tweezers [14].

1.1.2 Applications

Optical tweezers are a flexible technique used in various sub-fields of physics, chemistry and biology as shown in the following non-exhausting list.

Biological motors

Kinesin, like many other enzymes, is a linear motor that converts the energy of ATP hydrolysis into mechanical work in order to move along polymer substrates binding to successive sites along the substrate [9]. Svoboda and colleagues aimed to verify if the kinesin motion follows characteristic steps or if the advancement has a discontinuous behaviour. This observation was achieved thanks to optical trapping technique with a high precision of position detection. The authors captured silica beads bound to kinesin molecules deposited on microtubules stuck on a coverslip. Thus it was possible to observe the motion of kinesin motors as the bead moved away from the centre of the trap and to estimate their step size to be 8 nm.

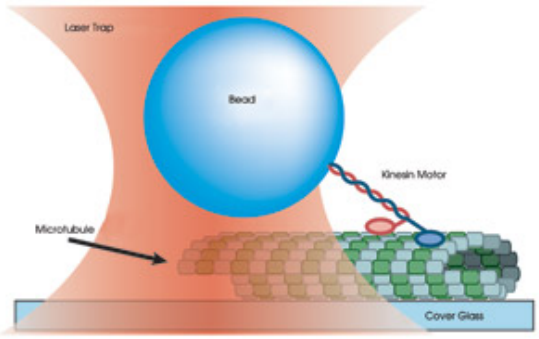

Figure 1.5: Trapped bead bound to one end of a kinesin molecule [19].

Another single-molecule mechanical measurement was performed using two traps in a three-bead geometry as shown in figure 1.6. A single actomyosin complex power stroke, a mechanism allowing the muscle contraction, was studied [10]. Myosin changes its conformation generating force and movement. In this research two optical traps were used to trap two beads holding an actin filament in the proximity of a myosin molecule attached to the third bead stuck on a surface. The position of the trapped beads was then monitored in order to obtain a force-extension diagram and to measure the tension resulting from the elongation of the filament.

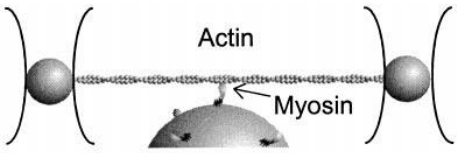

Figure 1.6: Three-beads geometry used to perform single-molecule mechanical measurements from actomyosin [10].

Measurements involving DNA

Using two counter propagating beams it was possible to measure tension in a DNA molecule in the following way: two beads were attached at the extremities of the DNA molecule, one of the two was held using a micropipette inside a flow chamber while the other was trapped optically [11]. The micropipette was moved in order to vary the tension in the DNA molecule and so it was possible to measure both the displacement between the two beads and the force acting on the molecule.

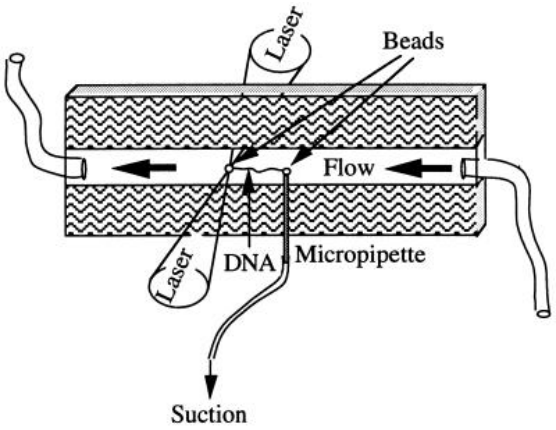

Figure 1.7: Sketch showing the geometry used to make the measurement in the flow chamber [11].

Manipulation of Viruses and Bacteria

Ashkin demonstrated the possibility of trapping and manipulating individual tobacco mosaic viruses and oriented arrays of viruses using a single beam gradient trap [4]. The author noticed that it was possible to discriminate the position and the orientation of a virus, once trapped. Moreover the virus stayed intact after being trapped. In addition, it was shown that *Escherichia coli* bacteria had no apparent damage at low power beams (1-6 mW), however, they shrank because of the optical damage at a higher laser power ($\sim$ 100 mW).

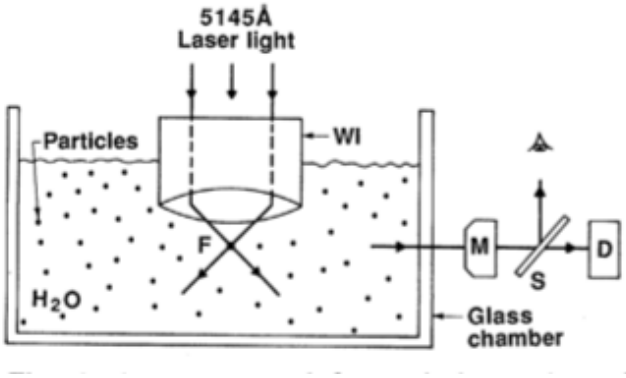

Figure 1.8: Apparatus used by Ashkin for optical trapping of viruses and bacteria [4].

Cells and optical tweezers

A measurement performed on living cells using optical tweezers was to quantify the elastic properties of red blood cell ghosts [20]. Two adhesive beads were attached in diametrically opposite positions on the cell membrane. One of the beads was held in place by the first trap, while the other was moved using the second trap. This movement induced a tension in the cell which was monitored through the displacement of the other bead giving the information about the force-extension curve and the elasticity of the cell membrane.

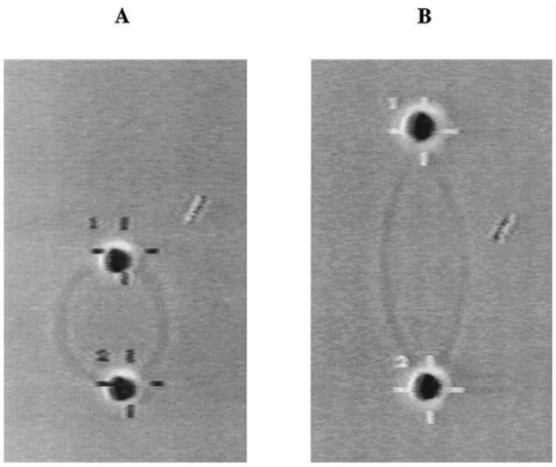

Figure 1.9: Geometry of the experiment using a red blood cell ghost attached to the beads held in two optical traps before (A) and after (B) the stretch [20].

Another type of experiment performed on cells using optical tweezers aimed to measure the tether force between the cell membrane and a probe microsphere [21], [22]. In particular the tether, which is a nanotube of plasma membrane lipids, was formed by laying for some seconds in physical contact the trapped bead and the cell, which was stuck on the coverslip surface. Then, by moving away the cell, it was possible to register the displacement of the bead from the centre of the trap and therefore the forces exerted by the membrane tethers.

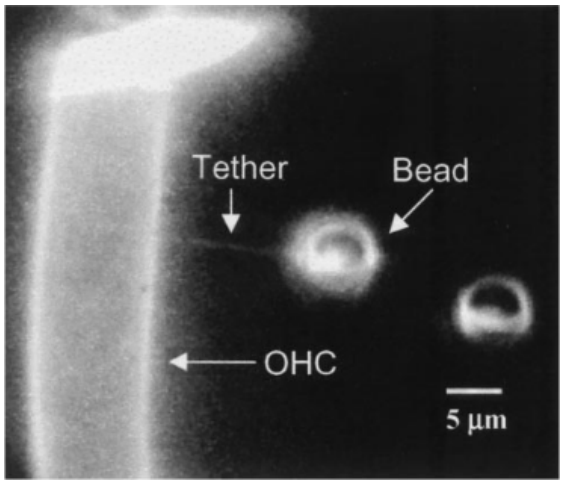

Figure 1.10: Fluorescence image of the experiment showing the tether between the outer hair cell (OHC) membrane and a polystyrene bead [21].

Photonic Force Microscope

Photonic Force Microscope (PFM) is a three-dimensional scanning probe micro-

scope based on optical tweezers [23]. This type of microscope evolved from the Atomic Force Microscope (AFM) with the idea of substituting a solid cantilever and its tip with optical tweezers and a trapped object, respectively. Thermal position fluctuations of the probe in the PFM are sensibly larger than the motion of the cantilever of the AFM, however these fluctuations provide useful information on the local environment. The main advantage of the PFM is the ability to apply sub-piconewton forces allowing imaging of soft substrates. In comparison for stable imaging with the AFM piconewton forces are required which can damage soft samples therefore only stiff structures are visible [23]. This particular application will be extensively analysed in the following chapters.

1.2 Physical principles

In general, an optical trap is formed by focusing a laser beam to a diffraction-limited spot with a microscope objective of high numerical aperture (NA) [3]. A dielectric particle diffusing freely in the proximity of the laser beam focus can be trapped. Once in the trap, it experiences an optical force due to the momentum transfer from the scattering of incident photons and to the spatial gradient of light intensity. As a consequence, a gradient force and a scattering force acting on the trapped object can be identified. In order to obtain stable trapping the axial gradient component must exceed the scattering component [24]. This condition is successfully achieved using an objective of high NA to focus the trapping laser beam to a diffraction limited spot in order to obtain a steep gradient in the light intensity. The equilibrium position of the particle is located slightly beyond the focal point, as a result of the balance between the two components of the force. Moreover, for small displacements ($\sim$ 150 nm), the restoring force is proportional to the offset from the equilibrium position, so the optical trap can be seen as a linear spring whose stiffness depends on the optical gradient, the laser power, and the polarisability of the trapped object [24]. Finally, the object size suitable for stable trapping is in the range between 20 nm and several micrometers, so not only a microsphere used alone or as a probe linked to a molecule of interest, but also single cells, organelles and lipid vesicles can be successfully trapped. The theoretical treatment can be described using two different regimes, the first is the Rayleigh approximation for particles whose size is much smaller than the wavelength of the light source and the second is the ray optics approach, useful when the diameter of the trapped object is much larger than the wavelength [25], [26]. The generalised Lorentz-Mie theory allows to describe and calculate optical forces acting on a particle of arbitrary size [27].

1.2.1 Rayleigh approximation, $R \ll \lambda$

When the radius of a sphere is much smaller than the wavelength of a trapping laser ($R \ll \lambda$) the sphere can be described as a point dipole $\mathbf{p}$, which is given by the following relation for a dielectric sphere in a uniform electric field [26]:

$$\mathbf{p}(\mathbf{r}, t) = 4\pi n_m^2 \epsilon_0 R^3 \frac{m^2 - 1}{m^2 + 2} \mathbf{E}(\mathbf{r}, t) \tag{1.1}$$

where $\mathbf{E}(\mathbf{r}, t)$ is the electric-field vector at the position $\mathbf{r} = (x, y, z)$, R is the radius of the sphere, n_m is the index of refraction of the surrounding medium, $m = n_p/n_m$ is the ratio between the refractive index of the particle and that of the medium. In this case the radiation pressure force experienced by the sphere can be evaluated using the Rayleigh scattering theory, distinguishing the two components as scattering and gradient, in the direction of light propagation and in the direction of the spatial light gradient, respectively. In figure 1.11 the forces experienced by a sphere in the Rayleigh regime are shown.

Scattering force

The particle acts as an electric dipole which, oscillating in time as does the electric field, radiates secondary or scattered waves in all directions. The scattering event contributes to changes both in the magnitude and in the direction of the energy flux of the electromagnetic wave. Therefore, a momentum transfer occurs and it is possible to identify a scattering force having the beam propagation direction. The force exerted on the particle is described by the following relation:

$$\mathbf{F}_{scatt}(\mathbf{r}) = \sigma < \mathbf{S}(\mathbf{r}) >_T \frac{n_m}{c} = I(\mathbf{r})\sigma\frac{n_m}{c}\hat{z} \tag{1.2}$$

where $\mathbf{r} = (x, y, z)$ is the evaluating position, $< \mathbf{S}(\mathbf{r}) >_T$ is the Poynting vector averaged over time, n_m is the index of refraction of the surrounding medium, c is the speed of light, I is the intensity of the laser beam, $\hat{z}$ is the unit vector directed as the light propagation, and σ is the cross section, defined as:

$$\sigma = \frac{128\pi^5 R^6}{3\lambda^4}\left(\frac{m^2-1}{m^2+2}\right)^2 \tag{1.3}$$

Gradient force

The gradient force arises from the fact that a dipole in an inhomogeneous electric field experiences a Lorentz force in the direction of the field gradient. Moreover, in the proximity of the focus of the trap there is a steep intensity gradient that induces fluctuating dipoles in the dielectric particle. The interaction of these dipoles with the electric field gives rise to the gradient trapping force [24]. So it is possible to describe an instantaneous gradient force as follows:

$$\mathbf{F}_{grad}(\mathbf{r}, t) = (\mathbf{p}(\mathbf{r}, t) \cdot \nabla)\mathbf{E}(\mathbf{r}, t) \tag{1.4}$$

writing $\mathbf{p}(\mathbf{r}, t)$ as in the equation (1.1) and knowing that

$$\nabla E^2 = 2(\mathbf{E} \cdot \nabla)\mathbf{E} + 2\mathbf{E} \times (\nabla \times \mathbf{E}) \tag{1.5}$$

where $\nabla \times \mathbf{E} = 0$ from Maxwell's equation, the gradient force is given by:

$$\mathbf{F}_{grad}(\mathbf{r}, t) = 2\pi n_m^2 \epsilon_0 R^3 \frac{m^2-1}{m^2+2}\nabla E^2(\mathbf{r}, t) \tag{1.6}$$

The particle experiences a gradient force averaged over the time so

$$
\begin{aligned}
F_{grad}(\mathbf{r}) &= < F_{grad}(\mathbf{r},t) >_T \\
&= 2\pi n_m^2 \epsilon_0 R^3 \frac{m^2-1}{m^2+2} \nabla < E^2(\mathbf{r},t) >_T \\
&= \pi n_m^2 \epsilon_0 R^3 \frac{m^2-1}{m^2+2} \nabla |E(\mathbf{r})|^2 \\
&= \frac{2\pi n_m R^3}{c} \frac{m^2-1}{m^2+2} \nabla I(\mathbf{r})
\end{aligned}
\tag{1.7}
$$

In conclusion, it can be noticed that the gradient force is proportional to the intensity gradient and when $m > 1$ (the index of refraction of the particle is greater than that of the surrounding medium) they point in the same direction.

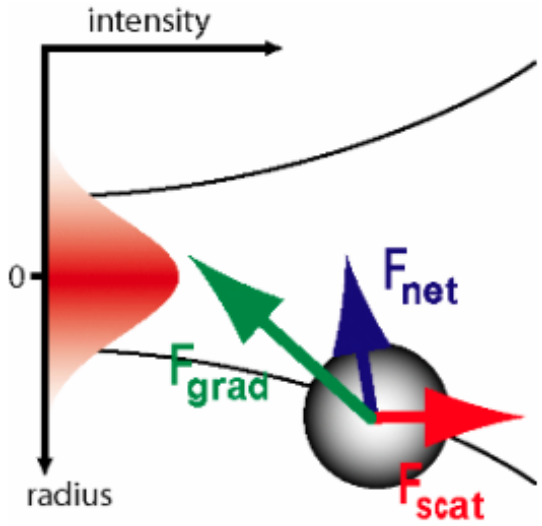

Figure 1.11: Representation of forces in the Rayleigh approximation, from [28].

1.2.2 Ray optics approximation, $R \gg \lambda$

In this regime the radius of the trapped sphere is much larger than the wavelength of the trapping laser ($R \gg \lambda$), so the optical forces can be described with ray optics [25]. The incident beam can be decomposed into individual rays impinging the sphere each with its proper position, intensity, and momentum so that each ray carries a momentum p_i which is proportional to its energy E and to the index of refraction of the medium n_i it passes trough:

$$
p_i = \frac{n_i E}{c} \tag{1.8}
$$

Therefore, the refraction of the incident light by the sphere corresponds to a change in the momentum carried by the light, so an equal and opposite momentum change is

experienced by the sphere. It is evident that if the sphere is centred with respect to the beam intensity gradient, the force experienced is only in the forward direction, parallel to the propagation of the light. Instead, if the sphere is displaced, the force acquires a perpendicular component whose direction depends on the index of refraction of the sphere. In fact, when the index of refraction of the particle is greater than that of the surrounding medium ($n_p > n_m$) the net force has the same direction of the light intensity gradient, otherwise ($n_p < n_m$) the net force is in the opposite direction. In figure 1.12, the forces experienced by the sphere for a Gaussian beam and for a index of refraction of the sphere greater than that of the medium are shown.

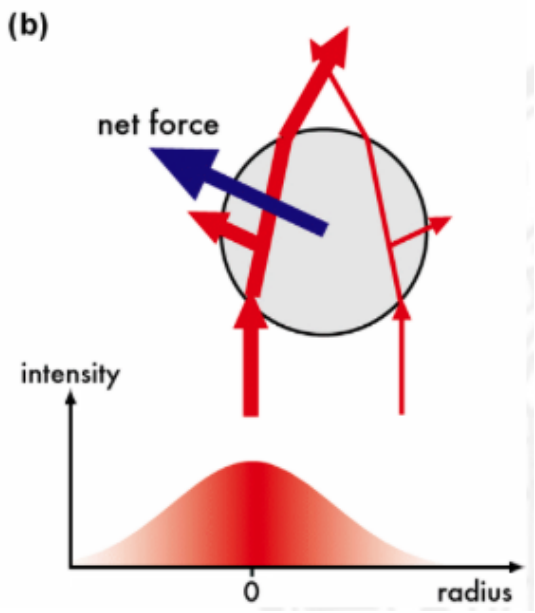

Figure 1.12: Representation of forces in the ray optics approximation, from [28].

1.2.3 Generalised Lorenz-Mie theory $R \approx \lambda$

Finally, when the radius of the trapped sphere is comparable with the wavelength of the laser ($R \approx \lambda$) neither ray optics nor Rayleigh approximation is valid, but in practice, the majority of the objects interesting to trap fall into this intermediate size range ($0.1\lambda - 10\lambda$). The mathematical approach is described by the generalised Lorenz-Mie theory (GMLT) where the radiation pressure forces are evaluated in terms of the transverse components and the longitudinal components of the cross section of the radiation pressure [26]. However, the more general description does not provide further insight into the physics of optical trapping [24].

1.3 Photonic Force Microscope

Photonic force microscopy (PFM) is a scanning probe microscopy technique (SPM), therefore it involves the use of a physical probe to scan the surface of a sample. It is based on optical tweezers, which allows to trap and manipulate the scanning probe in the three spatial dimensions. The displacement of the probe inside the trapping volume is defined, in absence of obstacles, by the brownian motion of the probe. When the trap is close to the sample surface, the trapping volume undergoes modifications due to the mechanical contact between the sample and the probe. The measurement of the displacement of the probe by interferometric tracking allows to follow its three dimensional trajectory and to obtain a topographic image of the scanned structure.

As mentioned in the previous section, the photonic force microscopy technique aims to perform topographical, as in the case of the atomic force microscopy (AFM) technique, and rheological studies. The main idea is to replace the mechanical cantilever of the AFM with a three dimensional trapping potential formed in a laser focus and the cantilever tip with an optically trapped object which can be a bead or a probe with a different shape. In figure 1.13 a schematic comparison between the two techniques is shown. The necessity of substituting the cantilever with an optical trap arises when the sample surface is particularly soft. In this case the tip of the mechanical cantilever is not able to follow the topographic details without causing a damage of the sample. Moreover, the application of forces of several tens of piconewtons is necessary for stable imaging. The use of an optical trap permits imaging of soft substrates while sub-piconewton forces are applied.

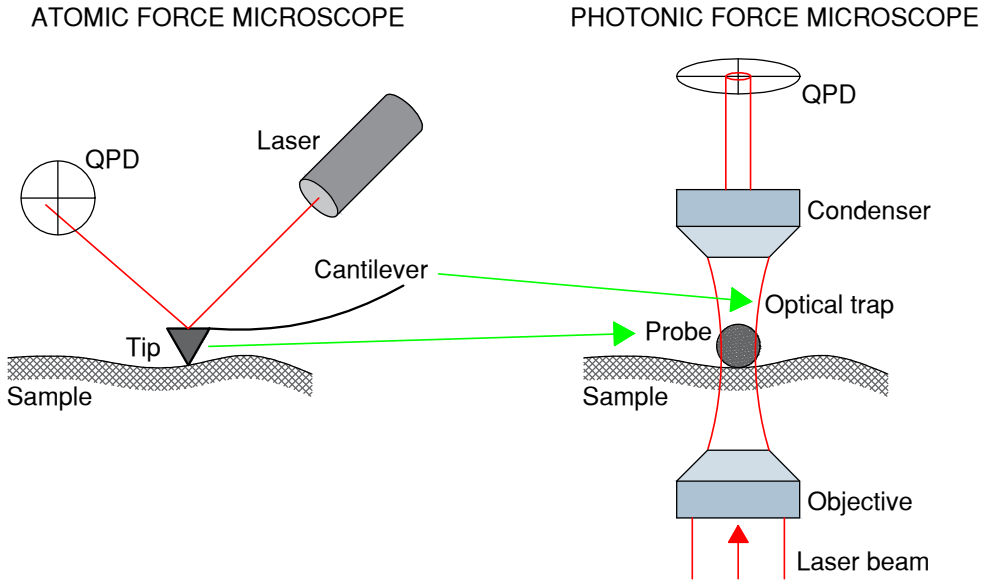

Figure 1.13: Comparison sketch between AFM and PFM. The cantilever and the tip are replaced by the optical trap and the trapped probe, respectively. The laser beam is directed to a quadrant photodiode (QPD) for the position detection.

In the PFM technique, the position fluctuations due to the brownian motion of the probe in the potential well formed by the optical trap are large with respect to the thermal motion of the AFM cantilever. The position fluctuations of the probe provide information about the local environment and interactions between the probe and the sample. However, when the forces applied by the trap on the probe are weaker than adhesion forces, the probe sticks to the sample through a non-specific interaction.

The first photonic force microscope was developed by Ghislain and Webb in 1993 by using a glass prolate particle as a probe in an optical trap [29]. The microscope was coupled to an expanded infrared laser beam (lambda 1064 nm) beam incident upon a high numerical aperture objective. The sample cell was scanned in x, y, and z using a piezostage and viewed by a differential interference contrast microscopy through the second microscope objective.

The probe experiences thermal fluctuations in the trapping potential, whose strength is determined by several factors such as the difference in the refractive index between the probe and the medium, the shape and the dimensions of the probe, the laser intensity and the intensity profile in the focal volume. However, the stiffness of the trapping potential is two or three orders of magnitude lower than the stiffness of the softest commercially available cantilever [23].

In the PFM the lateral position of the probe is measured by detecting the displacement of the beam from its central position by means of a position sensitive detector (PSD) or a quadrant photodiode (QPD). The lateral position can be video-tracked by using a fluorescent bead and recording the fluorescence intensity emitted by the fluorophores through a two photon excitation process [30]. The axial position is detected by measuring the interference intensity between the forward scattered light from the trapped particle and the non scattered laser light. These detectors provide the three-dimensional probe position with a resolution better than one nanometer at a temporal resolution in the microsecond range [23]. Often infrared lasers (980 nm, 1064 nm, etc.) are used since water and biological material in general have no significant absorption at these wavelengths. The PFM is based on a optical microscope with a usually high numerical aperture objective lens providing the image of the sample plane.

The PFM operates in a similar manner to the AFM contact mode, using forces range from hundreds of piconewtons down to tens of femtonewtons. Another possibility is the use of a feedback loop for force control in order to obtain a topographical scan at constant force. In this mode, lateral friction forces are evaluated, along with the force and error signals [31]. The size of the smallest distinguishable object is related to the diameter and the shape of the probe and to the thermal fluctuations of the probe inside the optical trap. Moreover, due to the Brownian fluctuations of the probe reaching hundreds of nanometers in a weak trapping potential, the PFM provides a thermal noise volumetric image [32]. By observing the spatial distribution of these fluctuations, which avoid stationary objects, it is possible to image a three dimensional structure, such as the structure of polymer networks with a resolution limited only by the precision of the detection system **ref** . In figure 1.14 the thermal noise image of an agar network is shown. It is worth noting that it is not possible to obtain these volumetric images using an AFM because the presence of the rigid cantilever does not allow the tip to explore the entire

volume around a three dimensional structure.

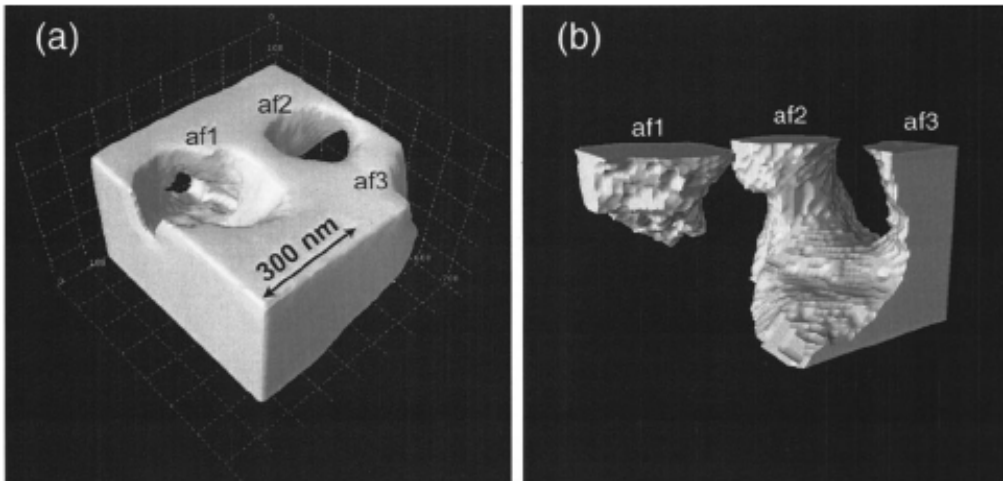

Figure 1.14: (a) Three dimensional thermal noise image of an agar network and (b) non accessible volume corresponding to the polymer fibers [32].

A method to improve the lateral resolution was presented by Friedrich and Rohrbach [33]. It is possible to obtain structural information with a resolution beyond the optical diffraction limit by subtracting the signal obtained by a raster scan using a trapped probe from the same scan with an empty trap [34]. The intensity of the signal measured in the back focal plane (BFP) of the detection lens during the empty trap scan is due to the interference between the laser and the sample, for each relative position of the sample and the trap:

$$I_{ES}(x,y) = |E_i + E_{sa}|^2$$

where E_i is the incident electric field and E_{sa} is the electric field due to the light scattered by the sample. The additional interference due to the presence of the trapped probe has to be considered. As a consequence, the measured signal intensity is

$$I_{PS}(x,y) = |E_i + E_{sa} + E_{pr}|^2$$

where E_{pr} is the electric field due to the light scattering of the probe. So, if we are interested in the interference due to the trapped probe, by performing a simple subtraction we obtain the tracking signal referred to the probe position:

$$|E_i + E_{sa} + E_{pr}|^2 - |E_i + E_{sa}|^2 = |E_i + E_{pr}|^2 - |E_i|^2 - 2Re\{E_{pr}E_{sa}^*\} \tag{1.9}$$

In the equation **??** the first term is the tracking signal, which provides the information on the probe axial position, the second term is an offset which is only due to the incident electric field, the third term is a remaining error due to the interference between the trapped probe and the sample. An evaluation of the magnitude can be performed by

considering the ratio between the amplitudes of the error and the tracking signal:

$$R = \frac{|E_{pr} E_{sa}^*|}{E_i E_{pr}^*} \tag{1.10}$$

from which it is possible to understand that the error depends on the scattering of the sample. This R factor is below 10% and it depends on the numerical aperture of the objective NA, on the refractive index of the medium n_m, on the trapping wavelength λ, and on the polarizability of the sample α_{sa}.

$$R \propto \frac{NA^2 n_m \alpha_{sa}}{\lambda^3}$$

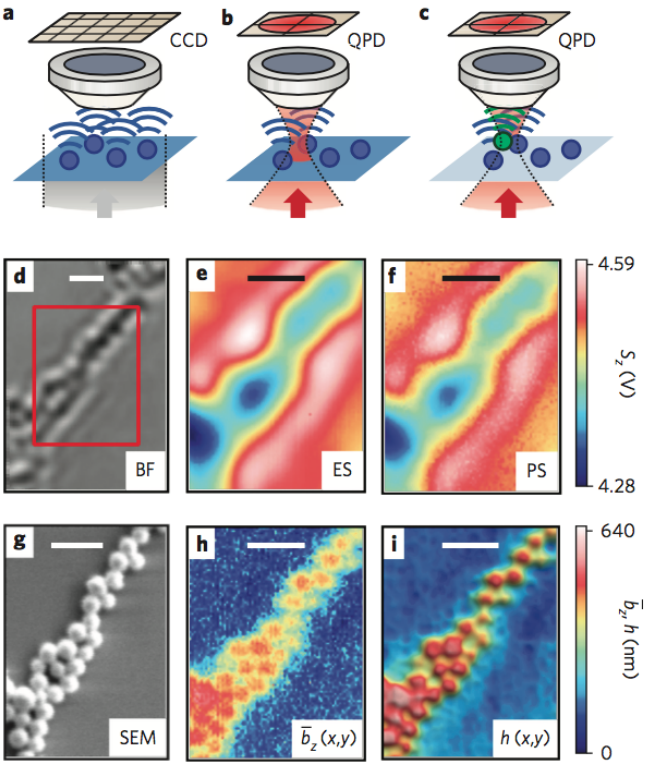

Figure 1.15: The effect of the subtraction between the scan with a probe (f) and the scan with an empty trap (e) can be observed in the image (h). Image (d) is the bright-field image and the (g) is a SEM image of the same area, while (i) is the image obtained by considering only the high energy fluctuations of the probe inside the trap [33].

It is worth noting that the correction becomes more important when the scattering of the sample is greater than that of the probe [34]. However, the position of the probe can be measured correctly only by considering the scattering disturbance due to the presence of the sample. In the following figures the influence of the correction on the axial position

of the probe due to the relative dimensions of the probe and the stuck bead is shown.

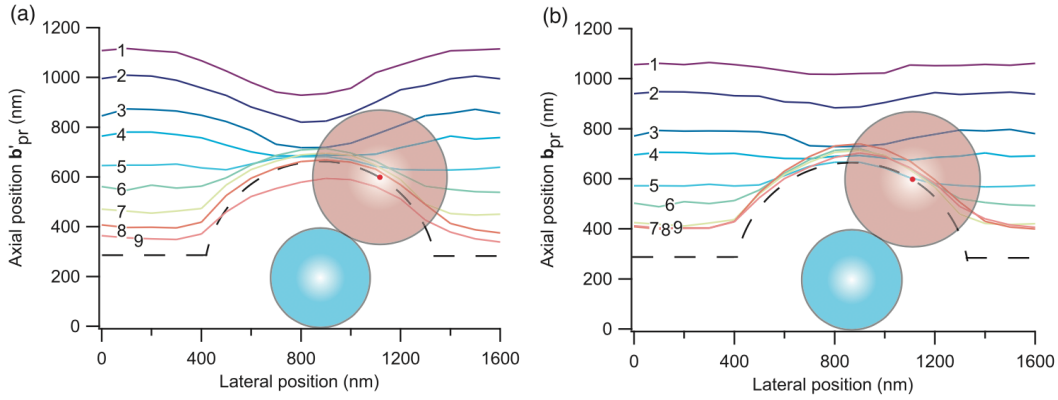

(a) (b)

Figure 1.16: Representation of the signal obtained by a linear scan over the surface structure by the optical trap. The probe is a 535 nm polystyrene sphere and the sample structure is a 400 nm silica sphere. (a) Measured traces at different heights above the surface. (b) Corrected probe traces. [34]

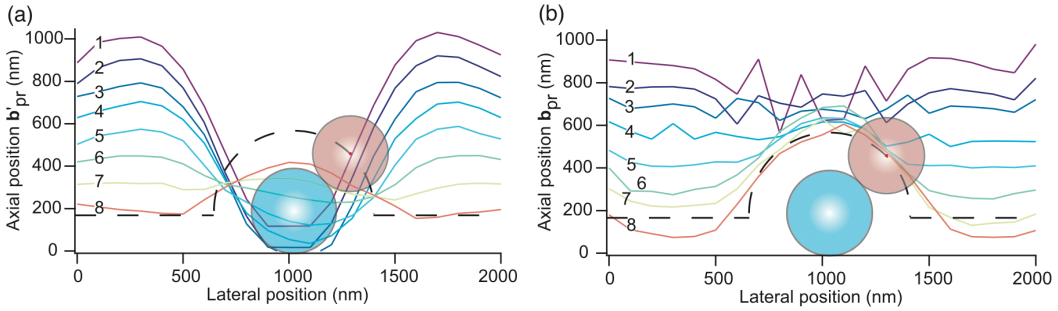

(a) (b)

Figure 1.17: Representation of the signal obtained by a linear scan over the surface structure by the optical trap. The probe is a 356 nm polystyrene sphere and the sample structure is a 400 nm silica sphere. (a) Measured traces at different heights above the surface. (b) Corrected probe traces. [34]

In particular, in figures 1.16(a) and 1.17(a) the measured traces of the probes are shown. In figure 1.16(a) the farther traces (1-3) seem to suggest a displacement of the probe with respect to the position of the sample. This effect is diminished when the difference with the empty trap is performed as it is shown in figure 1.16(b). It can be observed how the presence of the sample influences on the measured signal also when the probe is rolled in contact with the sample (traces 7-9). The effect of the disturbance due to the sample scattering is more visible when a smaller probe is used. In this case, in

figure 1.17(a) the trace 1, which corresponds to a linear scan far away from the surface of the sample, seems to represent a displacement of 800 nm for the trapped probe, which is of course not reasonable. After the correction, in fact, the traces present the expected trajectories as it is shown in 1.17(b).

This approach will be used in the following chapters for the data acquisition and analysis.

Materials and Methods

In this chapter two PFM setups are described, a double-beam PFM and a single-beam PFM. Several problems have arisen from the use of the double-beam PFM and have lead to the choice of the single-beam PFM. These problems are extensively discussed in the results chapter.

The optical alignment, and the sample preparation procedures are explained in the sections 2.2 and 2.4. The method for the optical trap calibration is extensively described in the section 2.3. The final section 2.5 is dedicated to the description of the data analysis and the image reconstruction.

2.1 Setup

In this section the setup of the photonic force microscope is described. In particular, two different setups are presented [35]. The first operates in a simultaneous double trap mode to scan the sample. This configuration allows to reduce the scanning time and decrease the inevitable influence of the sample drift between the scan with the trapped probe and the empty trap scan, which are described in the previous chapter. The second configuration uses a single trap for scanning both in the presence and in the absence of the probe. In both cases the description of the setup is split into two main parts: a laser unit and a detection unit. The laser unit provides a stabilized and collimated TEM_{00} mode of an infrared light. This is coupled to an inverted microscope to create an optical trap. The detection unit collects the light after the trap and brings it to a position sensitive detector (PSD) and to an intensity photo detector (PD) in order to track the lateral and axial positions of the trapped particle.
The detailed sketches of the setups are provided in figures 2.1 and 2.2.

2.1.1 Double-beam PFM

The double-beam PFM is a system with two optical traps whose signals having different polarizations can be distinguished and detected separately. In particular, the main trap is associated to the S polarization and the second to the P polarization.

The laser unit is based on a 3.5 W 1064 nm laser (*Azure Light System*). The light from the laser passes through a 1:1 telescope which is built by placing two lenses (L1, L2,

focal length f = 250 mm) in a standard 4f configuration. A pinhole (aperture diameter 600 μm) is placed in the 2f position of the 4f configuration in order to cut out high spatial frequencies. An acousto-optic modulator (AOM) is used to stabilize the laser power, with the help of a PID (Proportional Integrative Derivative) feedback controller, implemented in a FPGA board (Field Programmable Gate Array). The signal acquired by an InGaAs photo detector D1 is sent to the PID system. A wedged window W placed after the AOM deviates part of the beam to the detector, focused by a lens (L5, f = 40 mm) and, if necessary, reduced by a neutral density filter (OD = 1). An iris diaphragm cuts out secondary reflection from the wedged window. The beam that passes through the wedged window is then split in its S and P polarizations using a polarizing beam splitter PBS. The intensity of each polarization is controlled by a half-wave plate ($\lambda/2$) placed before and after the polarizer.

In the path of S polarization, the beam is expanded by using a beam expander (1:10), whereas in the other path, two lenses of different focal lengths (L3, f = 25 mm, L4, f = 250 mm) are used to build a telescope to achieve a beam expansion 1:10. The two expanded beams are then recombined by a non-polarizing beam splitter NPBS. They are slightly shifted in the horizontal direction one with respect to the other. The beams are directed to a mirror M7, which is part of the periscope that brings the expanded beams to the microscope and the detection system. The two traps are formed between two identical water immersion microscope objectives (numerical aperture NA = 1.2). The diameter of the expanded beam was chosen such to fill completely the back focal plane of the objective.

Bright field illumination is provided by a visible LED (660 nm or 470 nm) placed above the second mirror M9 of the telescope. Its light is focused by a lens through the condenser and the objective and brought at a CMOS camera by a mirror (M8) and a lens (L6). After the condenser, the mirror M9 directs the two beams to the detection unit. The two different polarizations are split again by a plate polariser PBS in order to distinguish the signals belonging to the two traps. The P-polarized beam is directed to an InGaAs photodetector (D2) which measures its signal intensity. The signal from the S-polarized beam is registered by a position sensitive detector (PSD) for lateral displacements and an InGaAs photodetector (D1) for axial displacements. The BFP of the condenser is imaged onto a camera CMOS2. The back focal plane detection is constructed by placing the principal detectors (PSD, D3, and CMOS2) in the planes conjugate to the back focal plane of the condenser with the help of the lens L7.

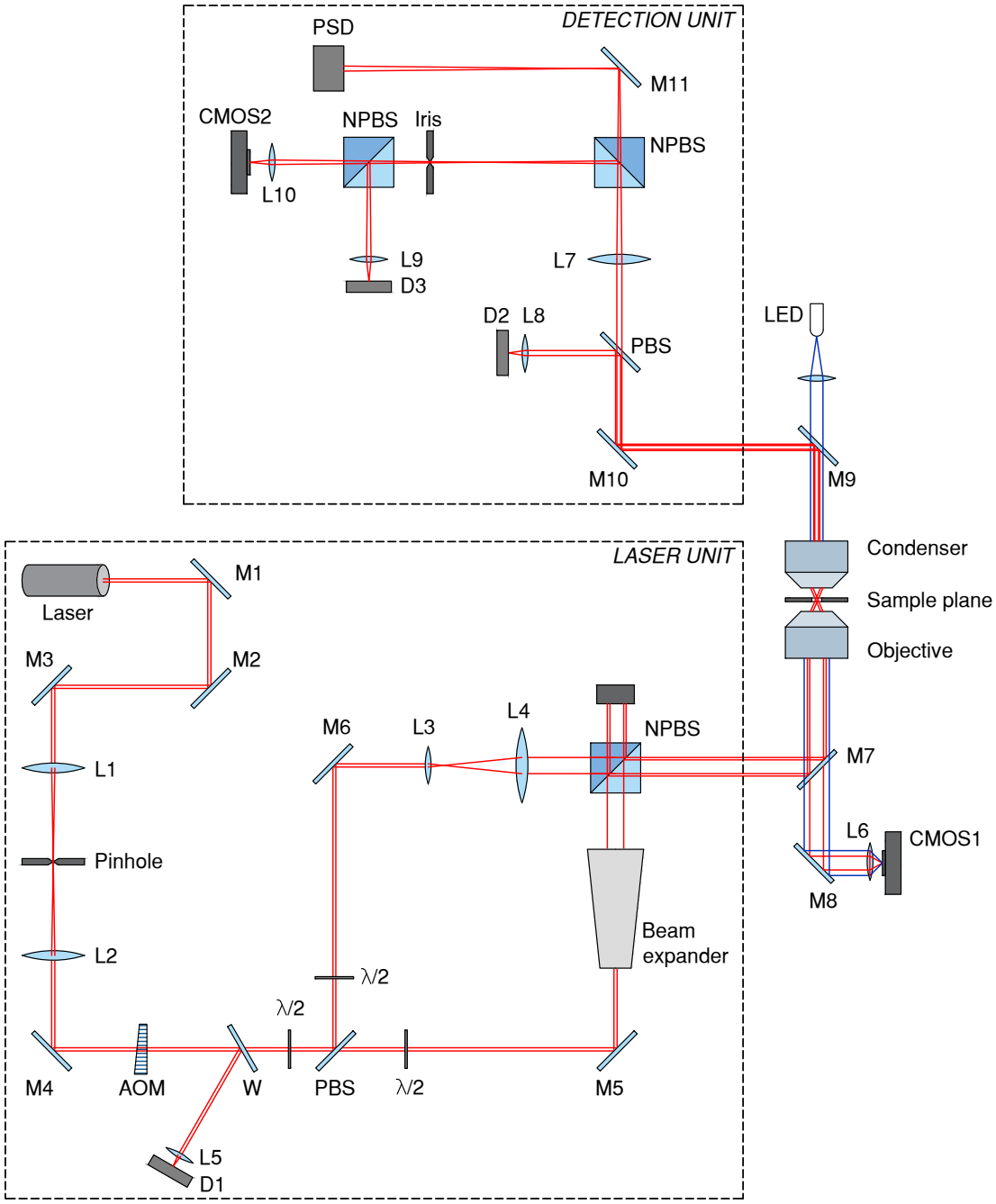

Figure 2.1: Double-beam photonic force microscope.

2.1.2 Single-beam PFM

The setup is modified with respect to the double-beam photonic force microscope. A half wave plate and a polarizer are positioned right after the laser, the path follows that

of the s-polarised beam of the previously described setup. Two additional lenses in the 4f configuration, were added between the NPBS and the mirror M7 in the laser unit. In the detection unit, the only change is the absence of the PBS and, consequently, of the detector D2. A sketch of the setup is shown in figure 2.2.

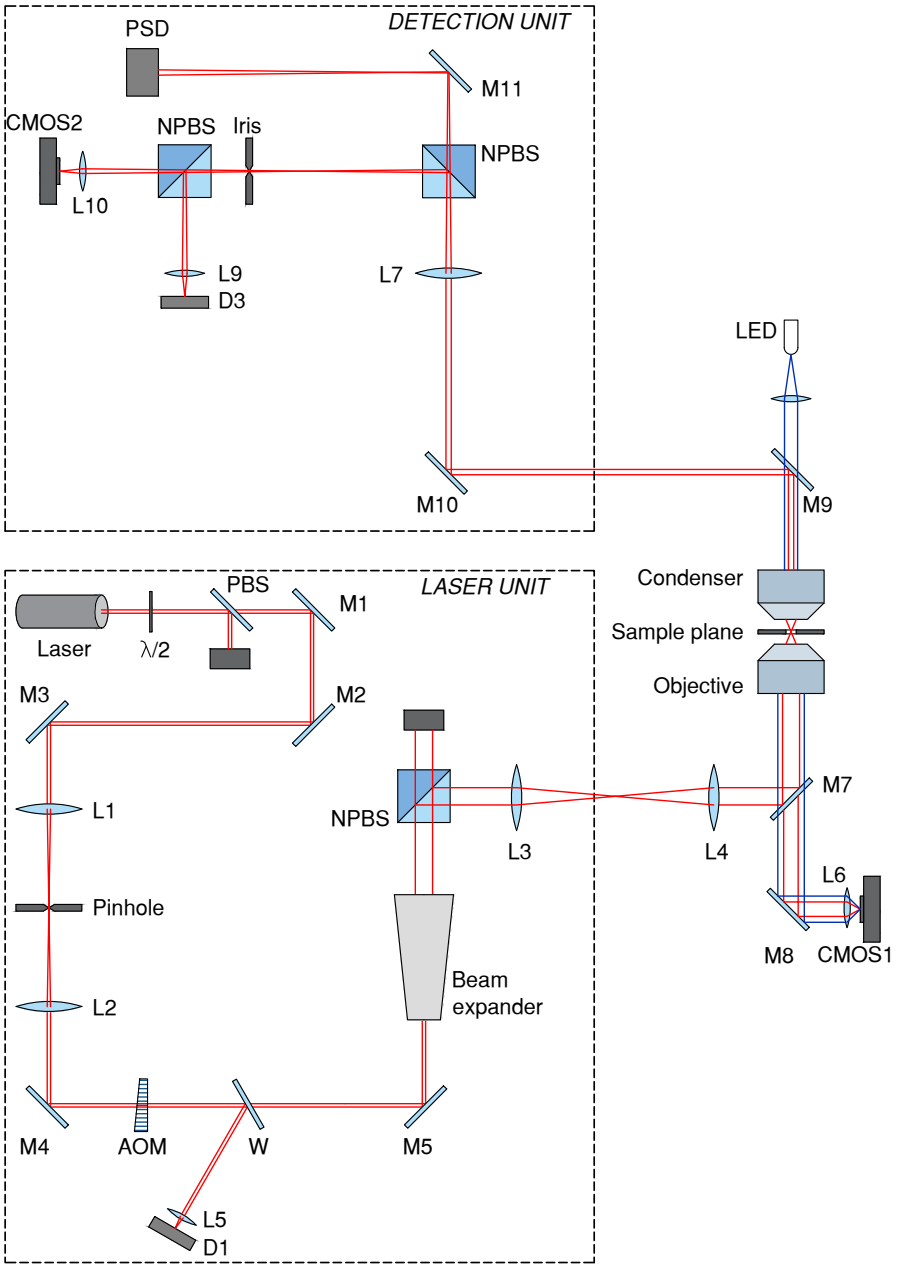

Figure 2.2: Single-beam photonic force microscope.

2.2 Alignment method

The aim is to direct the beam parallel to the optical table and along a straight line, in particular it is easier to follow the line of the table hole grid. The wavelength of the used laser is 1064 nm thus the alignment has to be performed using a detector card having absorption wavelength in the near infrared range and emission wavelength in the visible range. It is also possible to use an infrared CMOS camera for a finer alignment.
The first coarse alignment is performed using two diaphragms and the detector card. The two diaphragms have to be mounted at the same height. One of the two is placed close to the optical component to be aligned and the other is placed far away. Then, the height and the lateral shift of the optical component are adjusted until the beam passes through the first diaphragm. The second diaphragm is used to adjust the rotation of the optical component. The procedure is iterated until the beam passes through both diaphragms without being cut on any side. The schematic for the described procedure is reported in the figure 2.3. It is worth noting that the mirrors placed after the laser contribute to obtain a straight beam, parallel to the optical table. In fact, with two mirrors it is possible to control four degrees of freedom: two for the horizontal and two for the vertical tilt. This fact is particularly useful when the laser beam has to be coupled with a microscope in the periscope part: referring to the setup previously described, the NPBS and the M7 are used to control these degrees of freedom to direct the beam straight to the objective.
The same procedure is applied for the entire setup, taking particular care that the beam hits the centre of the optical components. Finally, when necessary the CMOS camera is used for a finer alignment. When the optical component is correctly aligned, the images of the two diaphragms are superimposed on the camera.

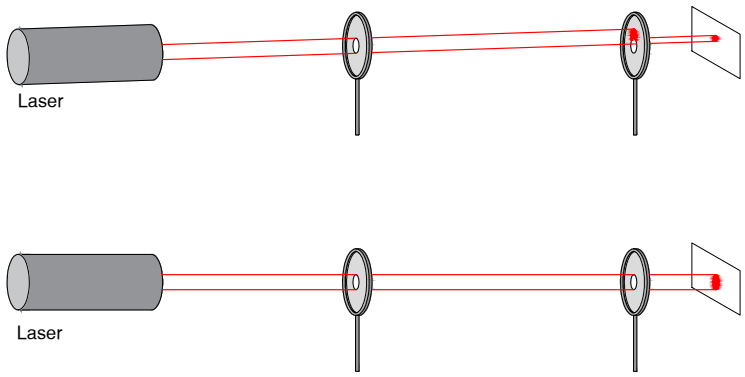

Figure 2.3: Schematic for the alignment procedure.

2.3 Calibration of optical tweezers

The calibration of an optical trap includes estimation of the following parameters: trap's stiffness, the Stokes viscous drag coefficient related to the trapped object, and the positional detector sensitivity. The high accuracy of the position detection is essential in OT. The positions are measured by registering the varying tension with a positional sensitive detector, where a conversion factor between units of voltage and units of distance is required. For small displacements, the force on a single axis in an optical trap is that of a Hookean spring so that $F = -\kappa x$ where κ is the stiffness and x is the displacement from the equilibrium point. Thus, force calibration is always reduced to the trap stiffness estimation. It should be noted that inertial forces and gravity are negligible for micron-sized objects due to the magnitude of the Reynolds number: $Re = va\rho/\eta \approx 10^{-5}$ where v is the fluid velocity, a is the particle size, ρ is the particle density, and η is the fluid viscosity.

2.3.1 Position detection calibration

As previously mentioned, the Hookean spring behaviour is valid for small displacements from the equilibrium point so that the linear region in which the force is proportional to the displacement can be identified. The measurement is performed with a stuck bead on the surface of a coverslip and the laser focus positioned at the height of the bead's centre. The piezoelectric stage is then moved so that the bead passes through the optical trap and the related detector signal is acquired together with the stage displacement. This measurement is then repeated for the three directions x, y, and z along the central axes of the bead. For a more complete position calibration a raster scan of the bead can be performed in order to cover the entire active region of the sensor [36].

The detector signal versus single axis stage scan through a stuck bead obtained for this calibration is reported in figure 2.4(a). The slope of the related curve returns the conversion factor β between voltage (V) and distance (μm). It is found through a linear regression fit of the linear region recognisable between the minimum and the maximum:

$$v = \beta x + q \tag{2.1}$$

where v is the voltage signal and x is the position associated to the piezoelectric stage motion.

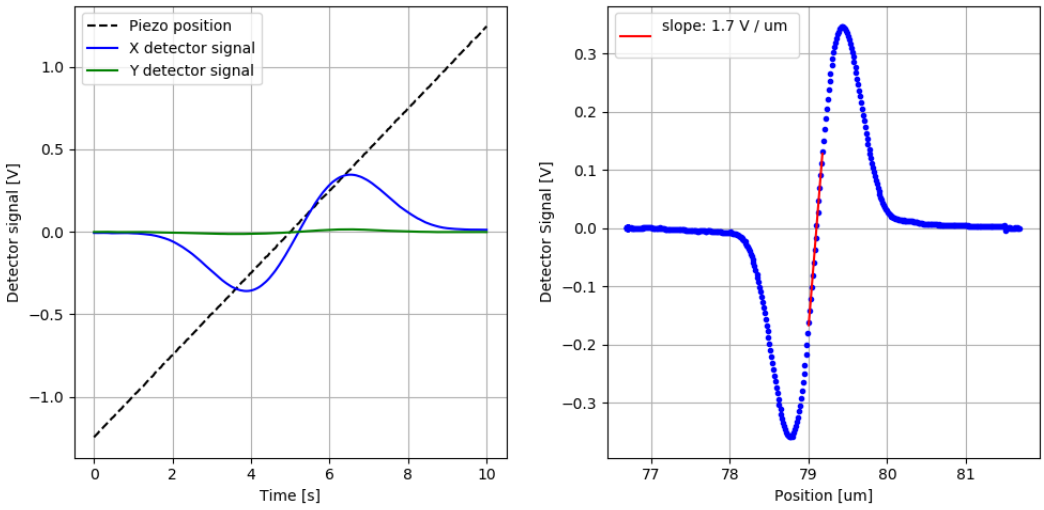

(a) (b)

Figure 2.4: (a) X and Y detector response to the motion of a bead through the laser focus (solid lines) performed by moving the piezoelectric stage (dashed line, the displacement on the vertical axis is represented in μm). (b) Positional detector calibration along the x direction for a 800nm polystyrene bead stuck on a glass coverslip, the resulted conversion factor is $\beta_{sens} = 1.7\ V/\mu m$. It is worth noting that the centre of the linear region is reached when the laser focus coincides with the centre of the bead.

2.3.2 Thermal motion analysis

This method is based on the measurement of the thermal motion of a bead of known size in the optical trap [36]. It allows estimating the Stokes drag coefficient and the stiffness of the optical trap by making an assumption on the geometry of the trapped object and knowing the positional sensitivity.
From the thermal motion of the trapped bead solely, one can obtain information on the trap stiffness. The variance of Brownian fluctuations is described using the *equipartition theorem* for an object in a harmonic potential having stiffness κ [24]:

$$\frac{1}{2}k_B T = \frac{1}{2}\kappa\langle x^2\rangle \tag{2.2}$$

This formulation is simple but unlike the power spectrum analysis it does not provide other information on the system beyond the trap stiffness. Besides, particular care should be taken using the equipartition theorem because variance is an intrinsically biased estimator, therefore, any additional noise contributes to the increase of the overall variance decreasing the estimated stiffness. In contrast, filtering the lower frequencies results in the increase of the estimated stiffness. It is interesting to notice that the positional variance is connected to the area under the power spectrum curve.
We decided then to use the following method, based on the power spectral density anal-

ysis, which allows estimating the previously mentioned factors.
The potential near the centre of the trap can be approximated as a parabolic well, therefore the object's dynamics is described by the Brownian motion in an harmonic potential [37]. The *power spectral density* (PSD), or power spectrum, of these fluctuations is approximately a Lorentzian for a bead of diameter d trapped in an optical well with a stiffness κ and a medium having a viscosity η. It can be written as

$$S(f) = \frac{S_0 f_0^2}{f_0^2 + f^2} \tag{2.3}$$

in units of distance^2/frequency, where f is the frequency, $f_0 = \kappa/2\pi\gamma$ is the corner frequency of the spectrum with $\gamma = 3\pi\eta d$ the Stokes drag coefficient for a sphere, and $S_0 = 4\gamma k_B T/\kappa^2$ is the zero-frequency intercept of $S(f)$ In addition, it is possible to calculate the medium viscosity η from the voltage power spectrum $S^V(f)$ multiplied by f^2. For $f \gg f_0$ the multiplied voltage power spectrum reaches a plateau, as shown in figure 2.5. The measurement of the plateau value P^V can be used to obtain the drag coefficient γ using the following relations [36]:

$$P^V = \beta^2 S_0 f_0^2 = \beta^2 \frac{k_B T}{3\pi^3 \eta d} \tag{2.4}$$

where the medium viscosity is given by

$$\eta = \frac{\beta^2 k_B T}{3\pi^3 P^V d} \tag{2.5}$$

thus, by recalling the formulation for the Stokes coefficient, we evaluate:

$$\gamma = \frac{\beta^2 k_B T}{P^V \pi^2} \tag{2.6}$$

As a consequence of the previous measurement, the trap stiffness is estimated independently by finding the corner frequency of the spectrum as follows:

$$\kappa = 2\pi\gamma f_0 \tag{2.7}$$

This method permits the evaluation of the Stokes coefficient γ and the trap stiffness κ, knowing the positional sensitivity obtained as shown in the section 2.3.1. The analysis is performed as explained in the following.

The bead is trapped in an aqueous medium and its Brownian motion is detected using the PSD. We fit the linear part of the power spectrum multiplied by the frequency with a polynomial of the first degree in order to find the plateau value P^V:

$$y = af + P^V \tag{2.8}$$

The a factor can be used as a control of the straightness of the plateau. This slope in fact should be approximately 0. The plateau value is used to estimate the drag coefficient, as

described in the equation (2.6), and the power spectrum is fitted with a Lorenztian

$$S = \frac{A_0}{1 + (f/f_c)^2} \tag{2.9}$$

where A_0 is the power spectrum value at zero frequency, and f_c is the corner frequency. Therefore, knowing the corner frequency and the drag coefficient, the trap stiffness can be easily evaluated from the relation (2.7). An example of the power spectrum and the multiplied power spectrum is shown in figure 2.5.

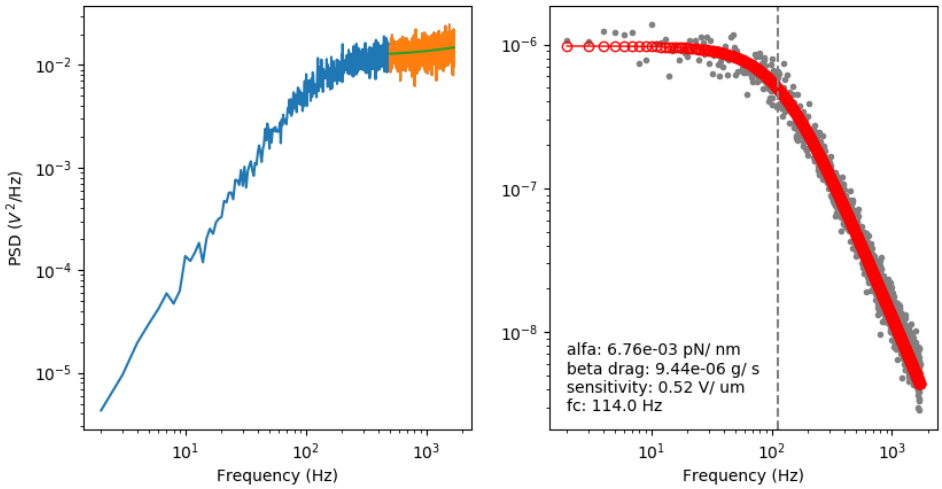

Figure 2.5: Multiplied power spectrum (left) and power spectrum (right) of a $1\,\mu m$ polystyrene bead. The detector sensitivity was evaluated separately using the position calibration method previously described. Corner frequency is $f_c = 114\ Hz$, Stokes drag coefficient along the z axis is $\beta_{drag} = 9.44 \cdot 10^{-6}\ g/s$, trap stiffness along the z axis is $\kappa = 6.76 \cdot 10^{-3}\ pN/nm$.

2.3.3 Sine modulation analysis

In the previous Section, the detector sensitivity and the trap stiffness are estimated with independent measurements and an assumption of the shape and the dimension of the trapped object are needed. To avoid these assumptions Tolić-Nørrelykke and co-workes developed a different calibration method combining the observation of the thermal Brownian motion of the trapped object as a response of the system to a known modulation [38].
A bead suspended in water is optically trapped and the stage supporting the flow cell is moved sinusoidally with a frequency f_{drive} and an amplitude A_{drive} so that the position of the stage is given by the relation

$$x(t) = A_{drive} \sin(2\pi f_{drive} t) \tag{2.10}$$

while the trap is at rest in the laboratory system. Thus, ignoring hydrodynamical and inertial effects, starting from the Langevin equation of motion for the trapped spherical bead it is possible to identify the PSD of the bead position as

$$S(f) = \frac{D}{\pi^2 \left(f^2 + f_0^2\right)} + \frac{A_{drive}^2}{2\left(1 + f_0^2/f_{drive}^2\right)} \delta\left(f - f_{drive}\right) \tag{2.11}$$

where δ is the Dirac's delta function and D is the diffusion coefficient given by the Einstein relation of diffusion:

$$D = k_B T/\gamma \tag{2.12}$$

The power spectrum in the equation (2.11) is given by the Lorentzian, due to the Brownian motion of the bead in the trap, and a delta-function spike at the modulation frequency. Therefore, the calibration factor related to the detector sensitivity in units of distance/volts is given by

$$\beta = \sqrt{W_{ex}/W_{th}} \quad [\beta] = V/\mu m \tag{2.13}$$

where W_{ex} is the measured power in the spike, in V^2, and W_{th} is the theoretical value, measured in m^2 and expressed as

$$W_{th} = \frac{A_{drive}^2}{2\left(1 + f_0^2/f_{drive}^2\right)} \tag{2.14}$$

Finally, once the conversion factor for the detector is determined, it is possible to estimate the trap stiffness experimentally using the following relation:

$$\kappa_{ex} = 2\pi f_0 \frac{k_B T \beta^2}{D^{volt}} \tag{2.15}$$

where D^{volt} is the diffusion coefficient measured in volts, and recalling the Einstein's relation for the diffusion coefficient (2.12), the drag coefficient is easily found:

$$\gamma_{ex} = \frac{k_B T \beta^2}{D^{volt}} \tag{2.16}$$

As we did in the previous method, we fitted the power spectrum using a Lorentzian curve, adding a δ function at the frequency corresponding to the drive frequency of the piezoelectric stage.

$$S = \frac{A_0}{1 + (f/f_c)^2} + C\delta(f - f_{drive}) \tag{2.17}$$

Given that we calibrate the trap using spherical objects we joined the thermal motion method and the sine modulation method. The detector sensitivity, in fact, is found using the plateau value of the multiplied power spectrum:

$$\beta = \left(\frac{3\pi^3 \eta P^V d}{k_B T}\right)^{\frac{1}{2}} \tag{2.18}$$

and so, knowing that $D = f_c^2 A_0 \pi^2$, we estimate Stokes drag coefficient and trap stiffness.

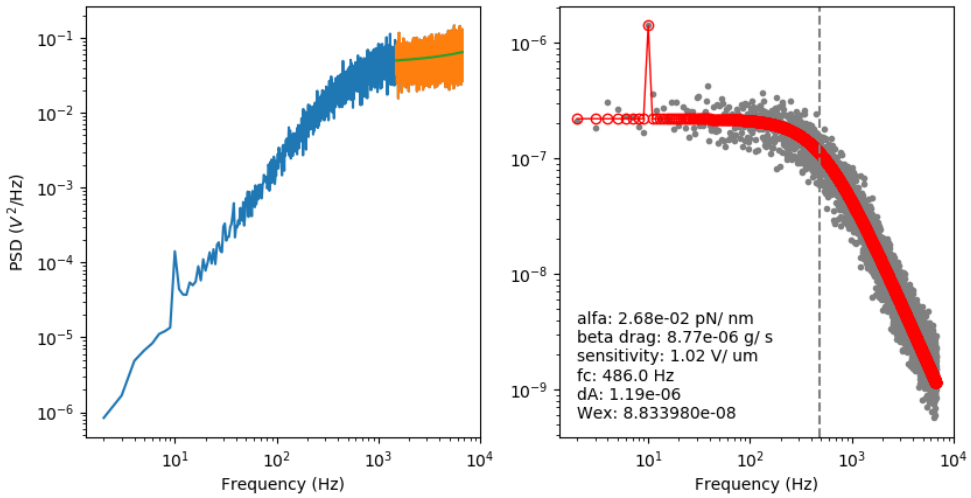

Figure 2.6: Multiplied power spectrum (left) and power spectrum (right) of a $1\,\mu m$ polystyrene bead. The sine modulation was applied along the y axis, the drive amplitude was $A_{dr} = 150\,nm$ and the drive frequency was $f_{dr} = 10\,Hz$. Corner frequency is $f_c = 486\ Hz$, Stokes drag coefficient along y axis is $\beta_{drag} = 8.77 \cdot 10^{-6}\ g/s$, trap stiffness along y axis is $\kappa = 2.68 \cdot 10^{-2}\ pN/nm$.

2.3.4 Allan variance

The Allan variance analysis is a method to measure the stability of the system, characterising the intrinsic noise in a system as a function of time [39]. The idea is to analyse a long sequence of data, averaging over time intervals of given length τ. Then, square the difference between the average $\bar{y}$ of the successive intervals and sum all of them, rescaling the sum by a factor 2(N-1), where N is the number of bins considered. This process is iterated through different τ values.

$$\sigma^2(\tau) = \frac{1}{2(N-1)} \sum_{k=1}^{N-1} (\bar{y}_{k+1} - \bar{y}_k)^2 \tag{2.19}$$

Using this method it is possible to have a quantitative measure of how much the average value changes at a particular τ. At short τ the Allan variance is dominated by the electrical noise in the system. In general, increasing τ the Allan variance decreases until a point at which it starts increasing again, due to mechanical instabilities in the output of the system. The best averaging time is given by the τ at which the Allan variance is minimised. In figure 2.7 the Allan variance curve at different acquisition frequencies and number of data points is shown.

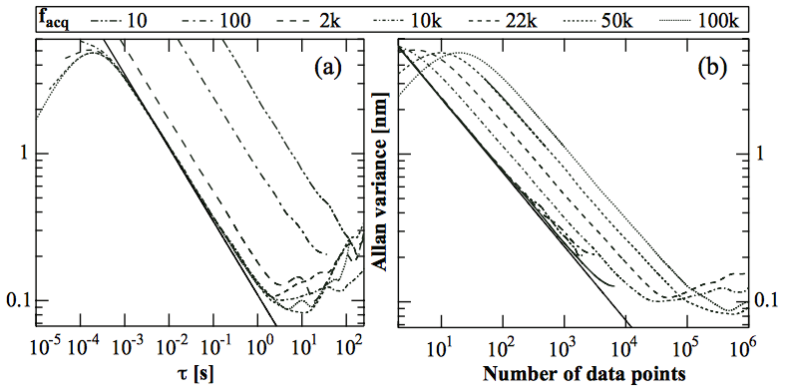

Figure 2.7: Allan variance dependance on the acquisition frequency (a) and on the number of data points (b) [40].

2.3.5 Calibration software

The two calibration methods described previously were implemented in a single dedicated software. It was developed in order to simplify and speed up the calibration process. We wrote the software in the Python programming language release 3.5 using its Tkinter module to create a Graphical User Interface (GUI). The GUI has two separate visually similar tabs. Each tab is dedicated to one of the calibration methods based on thermal motion analysis and on sine modulation analysis.

Thermal motion tab

The GUI tab dedicated to the first calibration method is shown in the figure 2.8. The are five main subsections described in the following paragraphs.

part A The user is asked to choose the data file and to put in several parameters such as the bead size, the viscosity of the medium, and the laser power. The two radio buttons allow the selection of the traps and related axes to be considered in the calibration. On the side there are six entry frames to display the output factors related to the calibration. Three of them are dedicated to the detector's lateral and axial sensitivities, and the other three display the estimated trap stiffness, Stokes drag coefficient, and corner frequency for a single chosen axis.

part B This section of the GUI is dedicated to the visualisation of the piezoelectric stage motion during the measurement ("Piezo. position" button) or, alternatively, of the bead position ("Det. position" button) and their distribution histograms. In particular, the bead position distribution is expected to be normal since the motion of the bead inside the trap is only due to the thermal fluctuations. As an example, the position plot of a 1 μm polysterene bead in the trap is shown in figure 2.9.

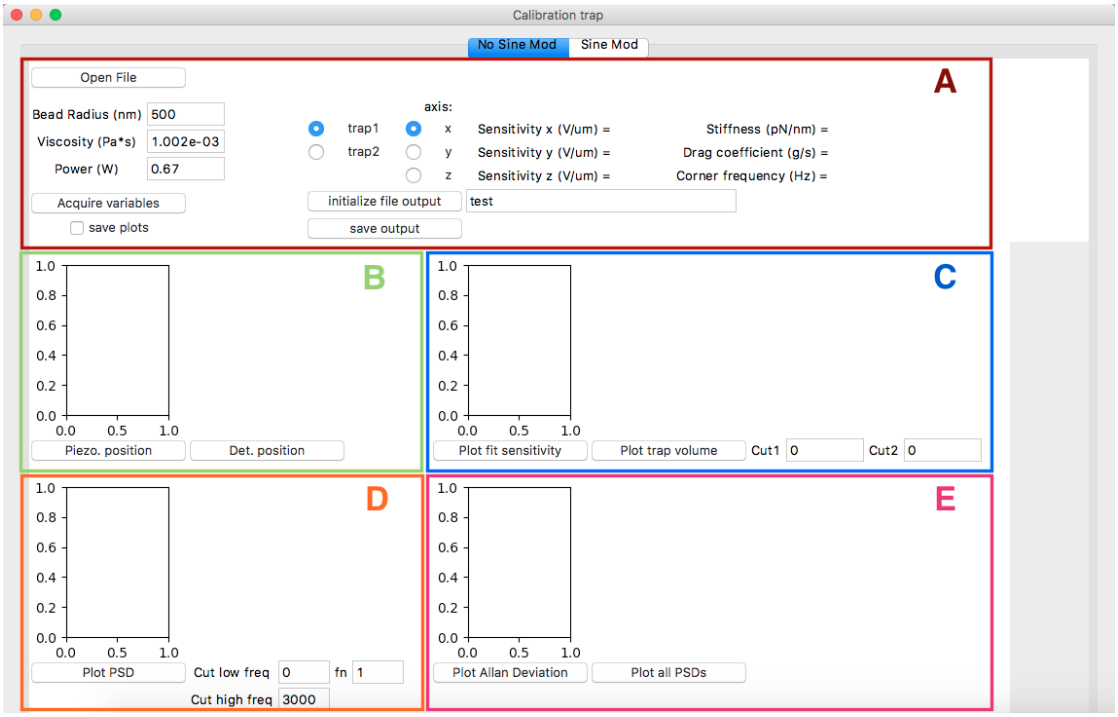

Figure 2.8: Calibration GUI tab1.

part C Before calculating the stiffness, we evaluate the sensitivity of the position detectors. To obtain the conversion factor for the three axes (x, y, and z), three independent measurements have to be done. Therefore, it is necessary to load three data files, each related to the calibration of a single axis. The slope of the fitted curve corresponds to the conversion factor, measured in $V/\mu m$, and is displayed in the designated output frame. It is useful to choose the number of points to cut, both in the beginning (cut 1) and in the end (cut 2) of the file. Since the acquisition system does not start or stop automatically together with the line scan, some extra points useless for the computation of the calibration coefficient are registered. Furthermore, with the button "Plot trap volume", it is possible to visualise the positions visited by the bead inside the trapping volume (in μm^3).

part D Using the conversion factor obtained in the **part C** it is now possible to evaluate the trap stiffness, the Stokes drag coefficient and the corner frequency. These parameters are calculated from the plotted PSD and the PSD$*f^2$ and are displayed in the **part A** of the GUI. Moreover, they are saved in a text file. In addition, there are several adjustable parameters that can improve the analysis. As input values the user can modify the starting point of the linear fit to obtain the plateau value of the PSD$\cdot f^2$ (f_N, integer), and the number of points to cut at high or low frequencies of the PSD. This is particularly useful because high frequencies are characteristic of the system's noise, such as electronic, which can disturb the quality of the Lorentzian fit. Whereas low frequencies evidence

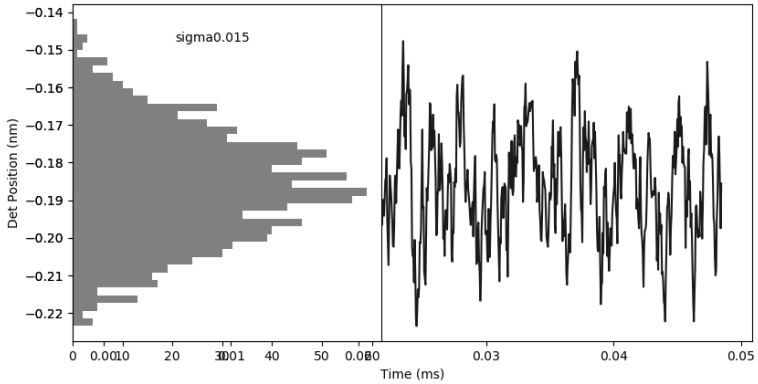

Figure 2.9: Detected position of a 1 μm trapped bead and its position distribution histogram.

the drift and influence the first part of the spectrum.

part E The last part of this tab is dedicated to a general quality evaluation of the system. It is possible to plot all the power spectra in a single graph without data deprecation for a better overview of the entire spectrum. Finally, the Allan deviation is plotted in order to determine the adequate acquisition time, as described in the previous section.

Sine modulation tab

The second tab of the GUI dedicated to the Sine modulation analysis is presented in figure 2.10 . Its four subsections are described in the following paragraphs.

part A and B The first two subsections of this tab are almost the same as in the previously described tab. The main difference is that the conversion factor for the positional sensitivity is extracted from the power spectrum instead of the curve obtained by the line scan over a stuck bead.

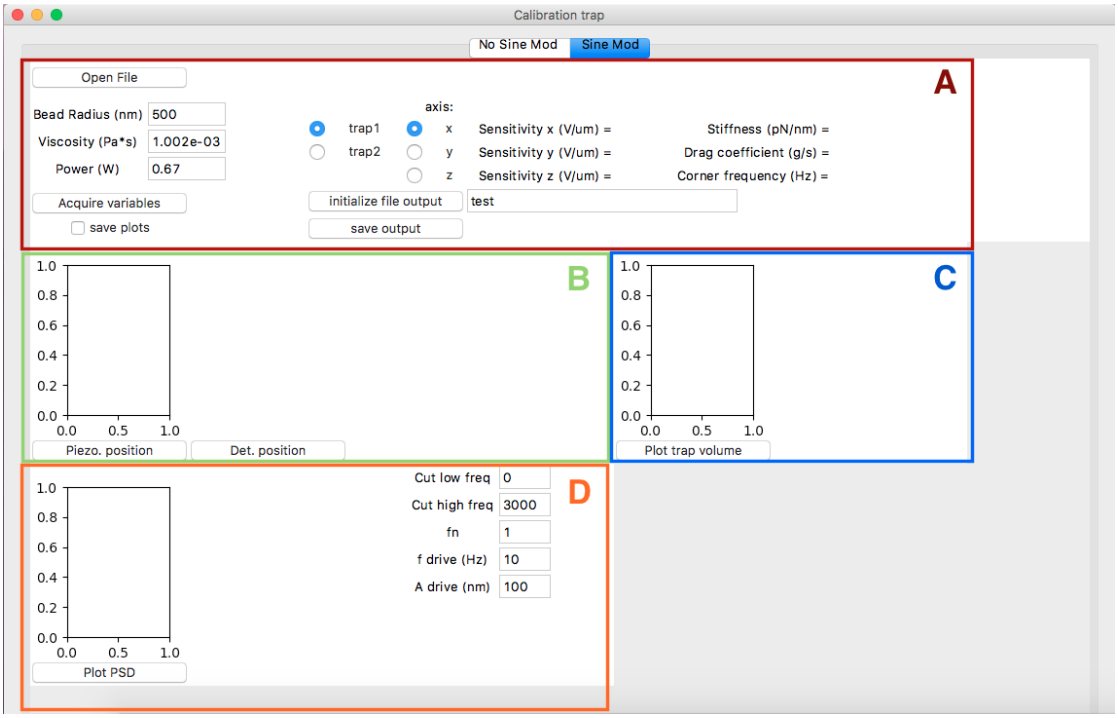

Figure 2.10: Calibration GUI tab2.

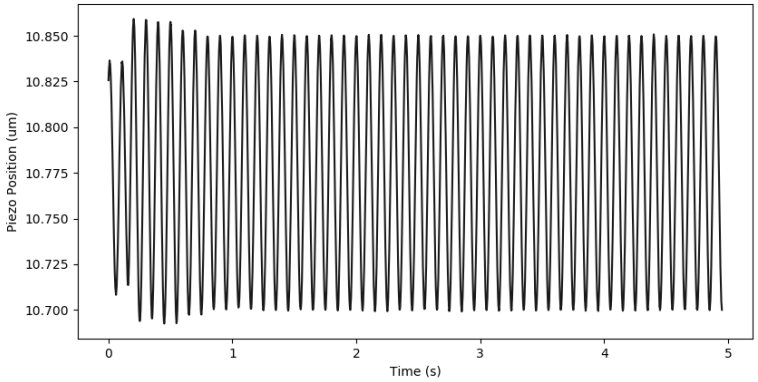

Figure 2.11: Typical trace of the piezoelectric stage positions during a sine modulation. The drive frequency is $f_{drive} = 10\,Hz$ and the amplitude is $A_{drive} = 150\,nm$.

part C Similarly, in this subsection the trapping volume can be plotted once the conversion factor is known.

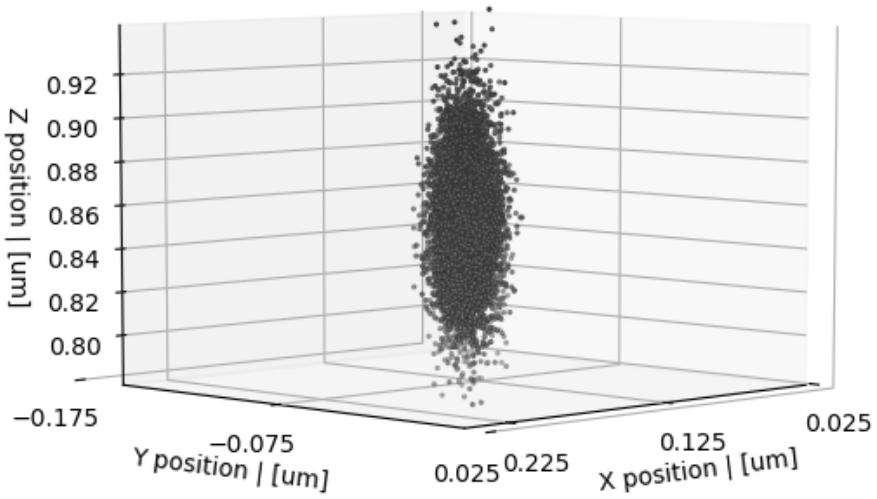

Figure 2.12: Example of trapping volume, the conversion factors for the three dimensions are $\beta_x = 0.77\,V/\mu m$, $\beta_y = 0.90\,V/\mu m$, $\beta_z = 0.35\,V/\mu m$.

part D As in the first tab, this part is dedicated to the PSD and the $f^2 * PSD$ plots. From this analysis the positional sensitivity, the Stokes drag coefficient, the trap stiffness, and the corner frequency are evaluated and displayed in the **part A**. These values can be saved in a text file initialised in the **part A**. The input parameters are the same as explained before: the fit's starting point f_N, the number of points to remove at high or low frequencies. In addition there are two parameters related to the sine modulation: the amplitude and the frequency at which the piezoelectric stage is driven.

2.4 Probes and sample description

A variety of probes was used for scanning, the standard probe being a spherical probe, usually with small diameter ($\sim$ 300 nm) in order to reach a high lateral resolution. The possibility that we are testing is the use of a cylindrical probe, with a sharp tip which, as it is explained in the section 2.4.1 should allow reaching narrower regions. In the section 2.4.2 a general procedure for the preparation of the sample is described and the variety of samples used are presented.

2.4.1 Probes

Two families of probes were used in the PFM. The first one is composed by polystyrene beads of different sizes (diameter range from 300 nm to 1 μm), suspended in a buffer solution. To prevent adhesion of the probe to the sample, we suspend the probes in the 5% isopropanol or 5% ethanol solution. Other possibilities are PLL-PEG or sodium chloride (5mM), which are used for biological samples.

The second one is composed by cylinder- or cone-shaped probes. The idea of using these types of probes is to reach a higher lateral resolution during the scan, without being limited by the diameter of the spherical probe. A sketch is reported in figure 2.13, the point of the tip can reach a narrower region compared to the sphere.

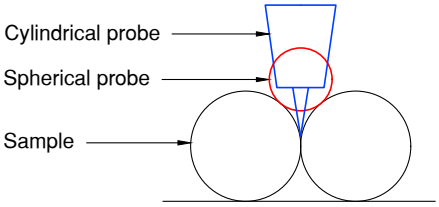

Figure 2.13: For geometrical reasons the cylindrical probe can reach a higher lateral resolution.

The cylinders used are fabricated by R. Desgarceaux and B. Charlot in the *Institut d'Electronique et des systèmes* (IES) of Montpellier. The fabrication consists of different steps, which are represented in the figure 2.14. The body of the cylinders is in quartz while the tip is in silicon dioxide (SiO_2), deposited on the quartz base and conveniently etched.

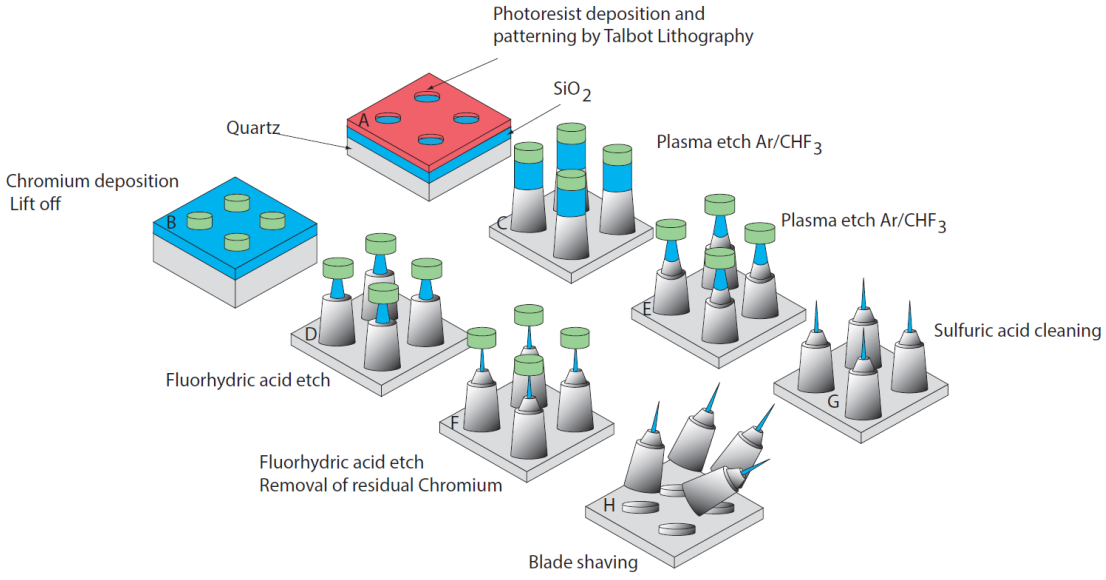

Figure 2.14: Cylinder fabrication process (image by courtesy of R. Desgarceaux).

Different sizes and shapes of cylinders have been tested. In figure 2.15 two SEM images of the different cylinders at the end of the fabrication process and after the blade shaving, are shown.

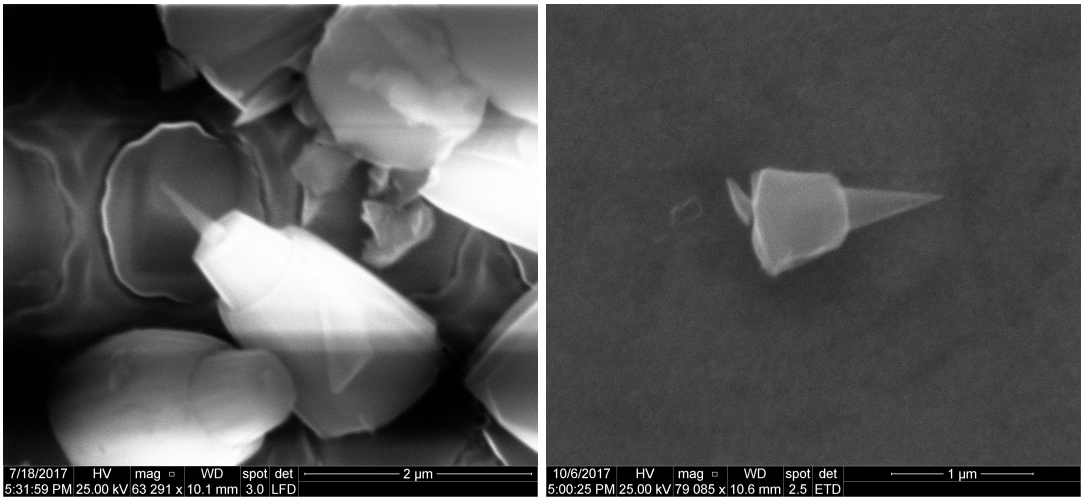

Figure 2.15: SEM images of the two cylindrical probes (images by courtesy of R. Desgarceaux).

2.4.2 Structures

There are two different kinds of structures used as a topographical sample. The first kind of structure was fabricated by lithography on the surface of a coverslip. In figure 2.16 an SEM (Scanning Electron Microscopy) image of a sample structure is shown. The diameter of this structure is approximately 15 μm and the height is around 280 nm, the lateral face of the structure is not orthogonal to the base surface of the coverslip.

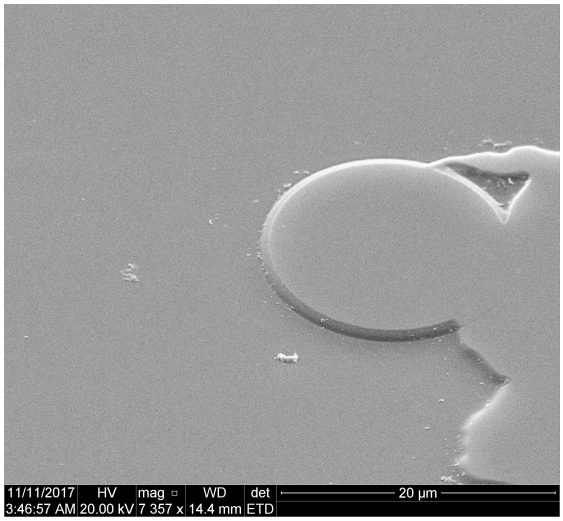

Figure 2.16: SEM image of the lithography structure (image by courtesy of R. Desgarceaux).

The second type of the structure was made of silica or polystyrene beads stuck on the coverslip surface. The beads are stored in a water solution. To stick the beads on the coverslip a droplet ($\sim 10\mu$L) was deposited on the glass and let dry at room temperature or using a heating plate to facilitate the evaporation of the water. Another option to stick the beads was to use 0.01% poly-l-lysine solution (PLL) to favour the adhesion of the beads on the coverslip. The disadvantage of this method is that during the scan the probe can adhere to the PLL layer. This can be overcome by covering both the probe and the sample with the 0.1 mg/ml poly-l-lysine polyethylene glycol (PLL-PEG). In figure 2.17 a SEM (Scanning Electron Microscopy) image of 300 nm polystyrene beads stuck on a coverslip is shown.

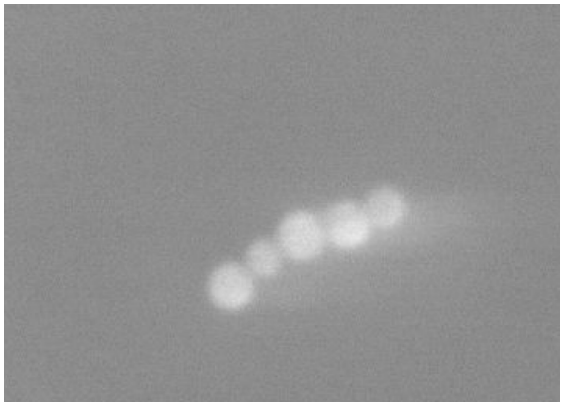

Figure 2.17: SEM image of the beads structure (image by courtesy of R. Desgarceaux).

The coverslip is cleaned by sonication in 1 M KOH for 60 minutes, to remove dust and other impurities which can cause adhesion between the probe and the glass surface or cause unwanted interferences in the laser signal. Then, the coverslip is rinsed in Milli-Q water. If adhesion to PLL is required, a drop of 10 μl PLL is deposited on the coverslip surface, spread on the whole surface with the help of a stripe of the Parafilm, and incubated for at least 15 minutes. Then, two stripes of the Parafilm are placed at the edges of the coverslip in order to have a separation between the bottom and the top coverslips (the lateral dimensions are 24 mm $\times$ 60 mm and 22 mm $\times$ 22 mm respectively, #1.5).In order to adequately attach the Parafilm to the glass it is necessary to melt it at 60C for few seconds on a heating plate. Then, to reduce evaporation in the sample it is possible to seal it using nail polish. A sketch of the sample is reported in figure 2.18.

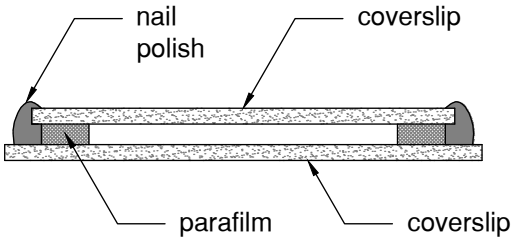

Figure 2.18: Sample sketch.

After that, using a pipette we injected the aqueous solution containing the probes. To prevent adhesion of the probe to the sample, we suspend the probes in the 5% isopropanol or 5% ethanol solution. Other possibilities are PLL-PEG or sodium chloride (5mM), which are used for biological samples.

2.5 Image acquisition

The images are acquired performing a raster scan over the region of interest of the sample. The coordinates of the starting point are passed to the piezoelectric stage, together with the length of the scan on both axis and the size of the single step. This way a pixel matrix is defined. For each pixel 800 values of intensity are acquired, at an acquisition rate of 40 kHz. This acquisition rate and number of intensity values for each pixel are chosen taking into account both the Allan deviation (in figure 2.19) and the entire acquisition time employed to complete a scan. The signal is acquired both in the axial and in the lateral directions.

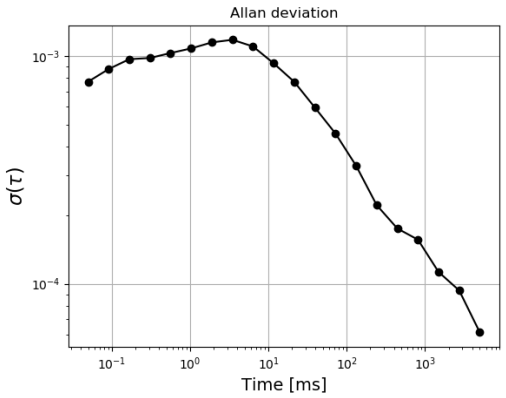

Figure 2.19: Computed Allan deviation for a cylindrical probe.

We wrote the scripts for the data analysis in the Python programming language release 3.5.

The final value for each pixel is obtained through the different strategies, depending if the signal belongs to the interference between the empty trap and the sample or to the presence of the probe in the trap. In the case of the trap without the probe the axial intensity signal z is averaged by taking the mean value of the 800 acquired values:

$$z = \frac{1}{N} \sum_i z_i \tag{2.20}$$

Concerning the axial intensity signal obtained in presence of the trapped probe, it is possible to consider both the mean value, as in the previous case, or the fifth (or tenth) quantile of the axial position distribution of the probe in the trap [33]. A quantile q of a sorted vector is defined as the value q/100 of the way from the minimum to the maximum of that vector. This has an important physical meaning: we already know that when the probe is in the bulk, its position distribution follows a Gaussian distribution because of the harmonic potential in the trapping volume. When a physical object is put in the trapping volume the position distribution undergoes a modification due to the fact that the potential is no longer harmonic on the entire volume. In figure 2.20 an example of the interaction between the trapping volume and an external potential is reported.

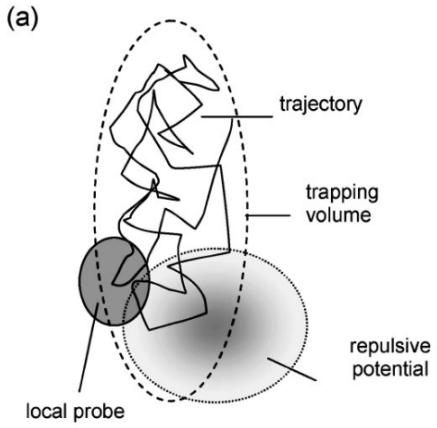

Figure 2.20: The trajectory of the fluctuating particle is related to both the optical trapping volume and the repulsive potential [41].

As a consequence, the mean value of the position distribution is shifted but the values corresponding to the position at which the probe is in contact to the object are the lower ones. Considering that our aim is to find a topographical image, we are interested exactly in these values. Looking at the position distribution, these values are represented by the minimum value of intensity but, in order to reduce the effect of outliers only due to electronic noise we decided to consider the quantile of this position distribution. In figure 2.21 the position distributions for a cylindrical probe in bulk and on a structure are shown.

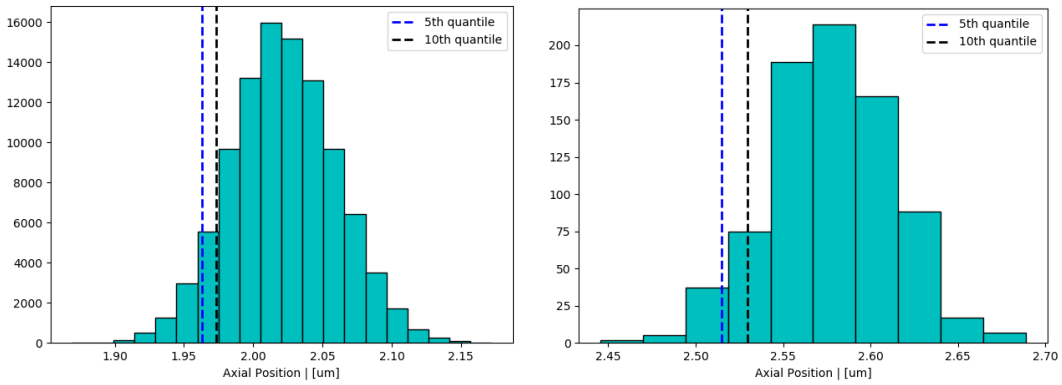

Figure 2.21: Position distribution for a cylindrical probe in bulk (a), and on a structure (b). The dashed lines highlight the fifth and tenth quantile of the position distribution.

Once the images are acquired with the trapped probe and the empty trap, the subtraction between these two has to be performed because of the reasons discussed in the section 1.3. An issue about this method is the inevitable drift of the sample between the acquisition of the two images, especially in the case of the single-beam PFM. In the case of the double-beam PFM also the distance between the two traps has to be considered. The adopted approach consists in cross-correlation of the two signals. The point at which the correlation is maximized indicates the distance between the two traps.

2.5.1 Cross-correlation based sub-pixel shift

Some preprocessing has to be done prior to the cross-correlation. It is worth noting that these operations are performed only to find the distance between the two traps, whereas the subtraction between the two traps is done with the unmodified data. The two images are visualized by defining a matrix of pixels, whose coordinates and axial values are defined corresponding to the piezo-stage positions and to the intensity value in that point.

These intensity values of both images are normalized to a zero-mean signal and unit variance by subtracting the mean value of the signal $< z >$ from the value of each pixel z_i, and dividing by the variance σ_z and the total length of the signal:

$$z_{norm} = \frac{z_i - < z >}{N\sigma_z} \tag{2.21}$$

Then, a Gaussian filter is applied to both images to blur them reducing the details. A Gaussian filter is a non-uniform low pass filter, characterized by a kernel which approximates a two-dimensional Gaussian curve. The degree of smoothing is defined by the standard deviation σ of the Gaussian. The kernel coefficient depends on the value of σ and at a higher σ corresponds to a greater blurring. The standard deviation used in the Gaussian kernel can vary depending on the considered signal, usually $\sigma = 1$. After having blurred both images, the resulting outputs are cross-correlated in order to find

the shift between one image and the other. The cross correlation C is defined, in the discrete form, as

$$C(x,y) = \sum_{i=0}^{W-1} \sum_{j=0}^{H-1} f(i,j)g(x+1, y+j) \tag{2.22}$$

where W and H are the width and the height of the image, respectively. So, the final output is a matrix of points shaped W+P-1 by H+Q-1, where P and Q are the width and the height of the second image. The maximum of the cross correlation corresponds to the value, in terms of pixels, of the shift between one image and the other. If the peak is localized in the centre of the cross-correlation matrix, the shift is equal to zero.

A method to obtain a better resolution in the shift of the image consists in performing a sub-pixel shift. The size of this shift can be obtained by fitting the cross-correlation matrix by a two dimensional Gaussian. The peak of the Gaussian provides the components of the shift in terms of fractions of pixels. Using this method it is possible to achieve a better precision in performing the subtraction. An example is reported in figure (b). The sub-pixel shift is performed by using a spline interpolation of the first order. In figure 2.19 a visualization of the shifting process is reported.

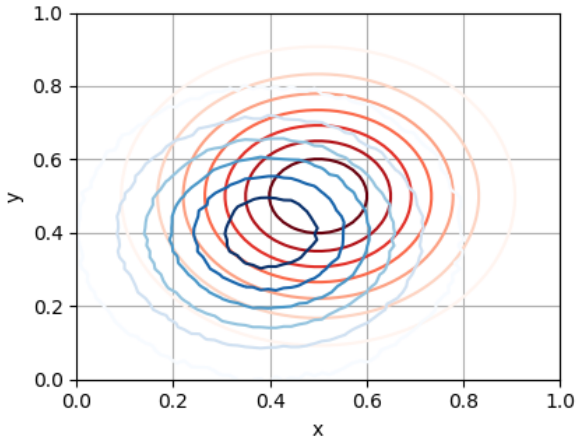

(a)

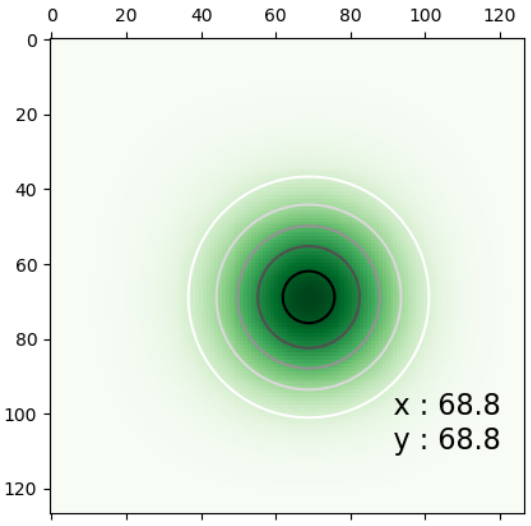

(b)

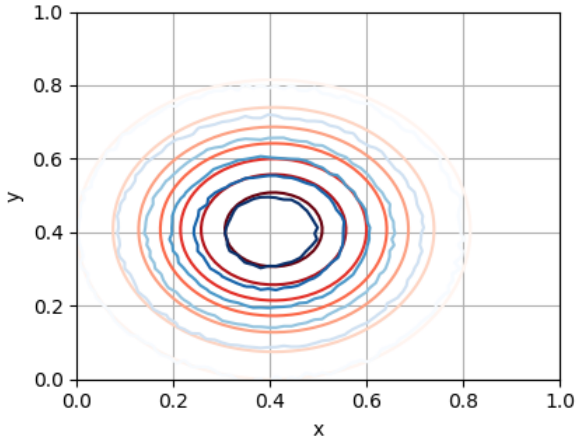

(c)

Figure 2.19: Synthetic data images demonstrating the effect of the cross-correlation based sub-pixel shift. In figure (b) the cross-correlation matrix fitted by a 2d Gaussian is shown. The size of the two images (in figure (a)) was 36 × 36 pixel so the central position of the correlation matrix is (64, 64). The centre of the fitted Gaussian is located at (68.8, 68.8) which means a shift between the two images of 4.8 pixels both in x and y, as shown in figure (c).

Once the operations described previously have been performed, a simple point by point subtraction between the images obtained from the scan in presence of the trapped probe and that with the empty trap can be done.

Results

In this chapter the results are presented. In the section 3.1, an approach to recognize the orientation of the cylindrical probe in the optical trap is introduced. The results of the scan measurements, the topographical image reconstruction, and the final image correction are presented in the sections 3.2 and 3.3 for the double-beam and the single-beam, respectively.

3.1 Orientation of the cylindrical probe in the optical trap

For a successful scanning, it is essential that the sharp tip faces and makes contact with the sample. However, this correct orientation of the probe is not the only one stable, as the cylinder can be trapped with the tip facing the wrong direction. To understand how the two orientations can be indisputably distinguished, we suppose that the cylinder has only two orientations inside the trapping volume because of geometrical reasons. For cylinders of dimensions greater than 1 μm, if the tip is long enough ($\sim$600 nm), it is possible to observe a shadow in the bright field microscopy image, as it is shown in figure 3.1.

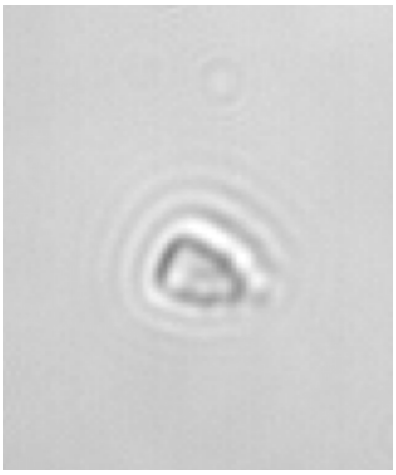

Figure 3.1: Bright field microscopy image of a floating cylinder with a tip.

However, in the majority of the situations, it is difficult to understand if the tip is oriented upwards or downwards with respect to the coverslip surface. In addition, when the tip is particularly short (the base of the tip can be approximately 100 nm) it is problematic to recognize the previously mentioned shadow. Moreover, if the illumination LED is misaligned, the bright-field image is distorted. This does not affect the measurement but it causes a different perception of the orientation of the probe.

We could identify two major features that indicate the orientation of the cylinder in the trap. The first one is the intensity level of the axial signal, and the second is the position of the contact-point of the cylinder with the surface of the coverslip. We perform an indentation measurement by moving the sample up towards the trapped cylinder and registering the axial signal. By plotting the latter versus the displacement of the piezo-stage, we analyse the indentation curve and recover the following parameters - the contact-point, the linear detection region length and its slope. The contact-point is determined by the axial position at which the intensity signal on the indentation curve starts rising over the fluctuations. The linear region is different, both in the length and in the slope for different orientations of the cylinder. When the aspect ratio of the cylinder is close to 1 or the shape of the cylinder approaches a cone, the cylinder flips to the side and then to the tip-up orientation at further indentation (figure 3.2).

Consider the examples of the indentation curves at different orientations of different aspect ratio cylinders together with the SEM image of each cylinder type that are given in the figures 3.2, 3.3 and 3.4.

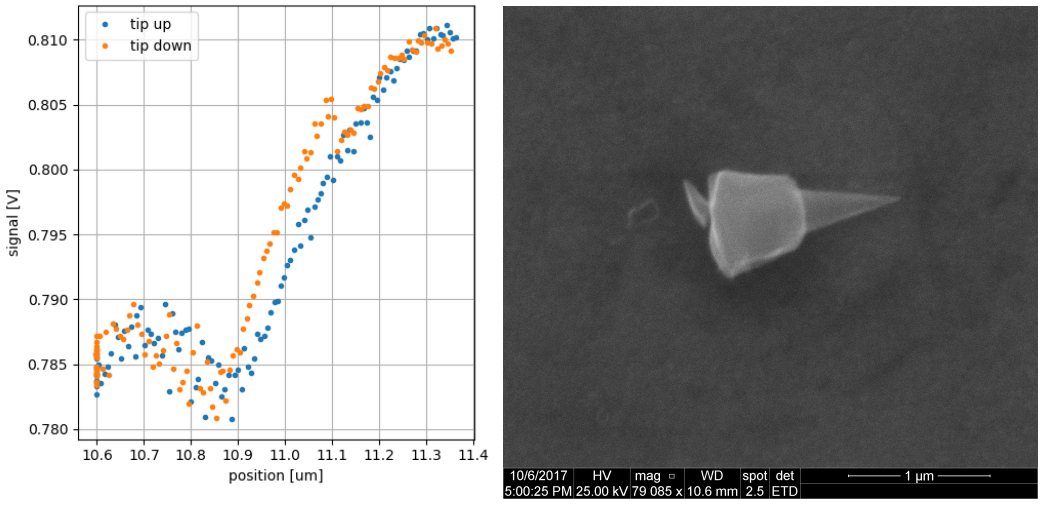

(a) (b)

Figure 3.2: (a) Indentation curve for a almost conical probe and (b) SEM image of this type of probe (image by courtesy of R. Desgarceaux).

In figure 3.3, we notice that the contact point for the two orientations is almost the same, which means that the tip was probably broken or absent.

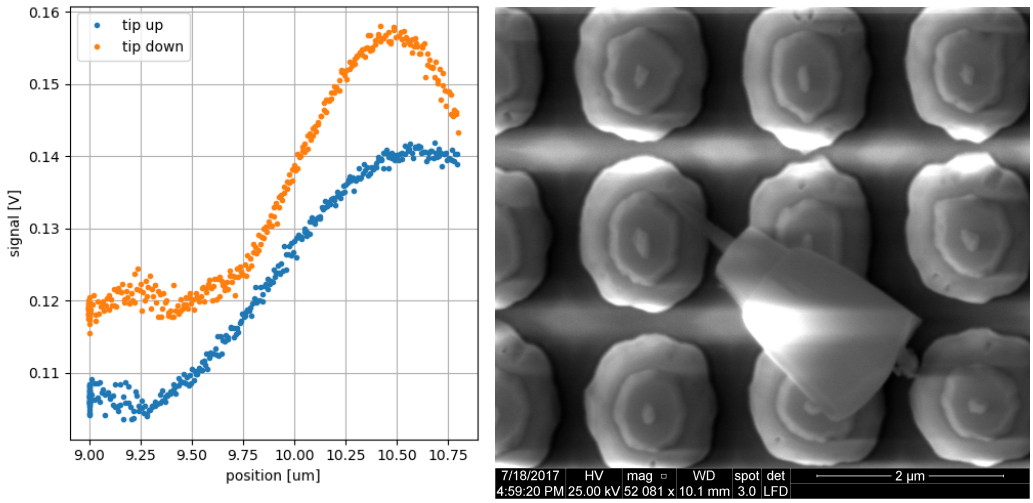

(a) (b)

Figure 3.3: (a) Indentation curve for a cylindrical probe and (b) SEM image of this type of probe (image by courtesy of R. Desgarceaux).

Finally, in figure 3.4 we distinguish clearly the two orientations. For the tip-down orientation the axial intensity signal is higher than that of the tip-up oriented cylinder, the linear region is smaller, and the contact point is reached sooner.

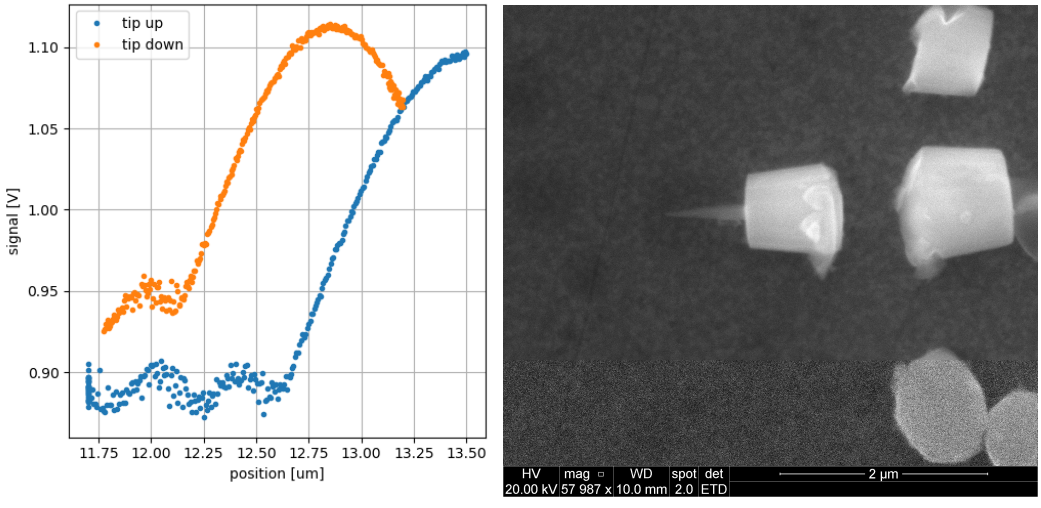

(a) (b)

Figure 3.4: (a) Indentation curve for a cylindrical probe and (b) SEM image of this type of probe (image by courtesy of R. Desgarceaux).

Depending on the orientation of the cylinder with a tip, its axial position in the trapping volume is different, namely, at the tip-down orientation the position of the centre of mass

is higher with respect to that of the tip-up. Therefore, the scattering forces are more intense for the first case for geometrical reasons and the axial intensity signal is higher. Moreover, the linear detection region of the indentation curve is shorter for the tip-down orientation. This is explained by the fact that the cylinder's centre of mass is further from the focus of the trap and the cylinder is pushed out sooner out of the trapping volume when approaching the coverslip. Thus, we suggest that the cylinder with the tip oriented downwards is the one positioned higher in the trap and reaching the contact point earlier in the indentation measurement.

In the figure 3.2 we observe the flipping behaviour of the almost conical microparticles. Indeed, at some critical axial position, the initially tip-down oriented cylinder first flips to the side and then to the tip-up orientation while remaining in the trap and followed by another linear region with the tip oriented upwards. The almost conical shape allows it to easily laying on the side and consequently turn to the most stable position instead of staying tip-down until it escapes from the trap.

In the following paragraph a suggestion for a method to estimate the length of the tip is proposed. This suggestion is based on a single measurement therefore this hypothesis is yet to be confirmed by repeated measurements on different cylinders. The rough estimation of the length of the tip could be done by using the graph shown in figure 3.5 in which the two orientation curves are plotted for a cylinder without a tip and in figure figure 3.4 for the same type of cylinder with a tip.

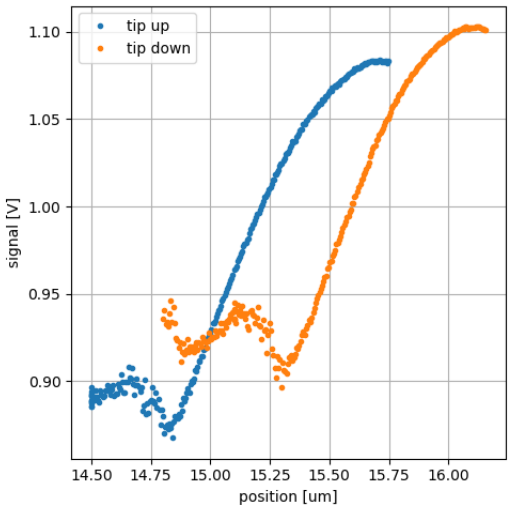

Figure 3.5: Indentation curve for a cylindrical probe without the tip.

We consider as zero-position the point of contact of the curves "tip up", which in principle should not be affected by the presence of the tip. The length can be estimated by taking the difference between the point of contact of the curves "tip down" in the two cases, referring to the zero-position. In this case, we find a difference of 750 nm which corresponds to the initial length of the tips on the wafer obtained from the SEM images

of 800 nm.
In figure 3.6 a schematic of the process is shown.

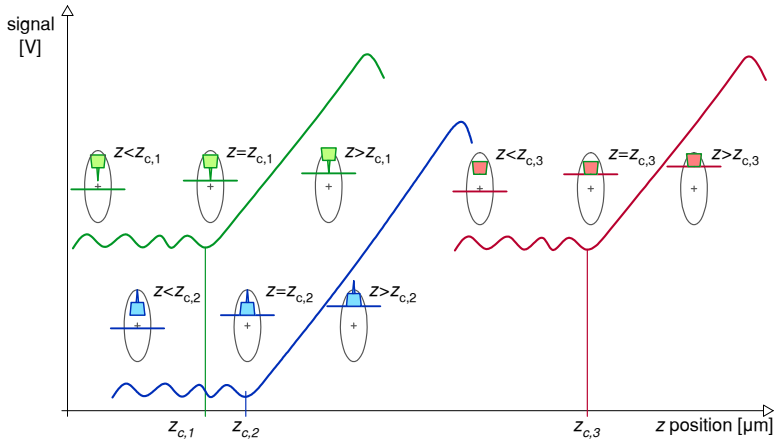

Figure 3.6: Schematic of the suggestion for a method for the cylinder tip length estimation.

3.2 Double-beam PFM

The first used approach for performing a scan is based on the double-beam PFM. The advantage is that it permits to complete a full scan (which means scanning the sample both in the presence and in the absence of the probe) faster than using only the single-beam configuration. This assures the reduction of the sample drift between the first and the second acquisition and, secondarily, it is time saving especially in the case of large structures.

In the figure 3.7 the images obtained from the scan of a sample composed from the 1 μm polystyrene beads is shown. The trapped probe was a 1 μm polystyrene bead. The difference in the Y position of the beads is equal to the distance between the first and the second trap.

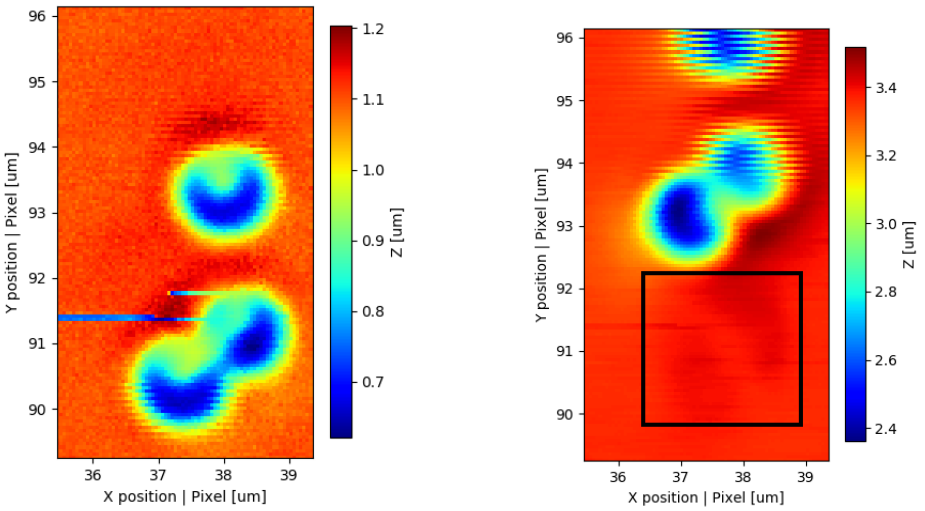

(a) (b)

Figure 3.7: (a) Image obtained in the presence of the probe; (b) Image obtained with an empty trap scan, in the squared region the shadow due to the crosstalk is highlighted.

In the figure 3.8 the result of the subtraction between these two scans is shown. In particular, the image obtained in the absence of the probe is taken as a reference. Therefore, the image reconstructed from the scan in the presence of the probe is shifted by the value obtained from the cross-correlation.

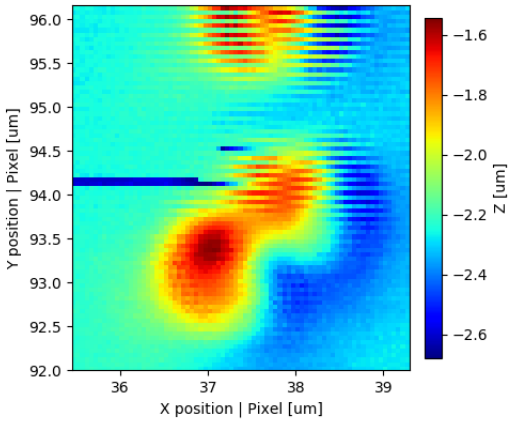

Figure 3.8: Effect of the subtraction between the scan in the presence and in the absence of the probe.

3.3 Single-beam PFM

Scan of a cluster of beads

The first trial done with the single-beam PFM aimed to reproduce the experimental conditions of the measurement performed by Friedrich and Rohrbach [33]. In this experiment they demonstrated how it is possible to reach a resolution beyond the diffraction limit, using the subtraction method discussed in the section 1.3. The sample is made of 353 nm silica beads, dried on a coverslip. The probe is a 300 nm polystyrene bead, floating in a 5mM NaCl solution. The piezoelectric stage is moved by steps of 40 nm and the acquisition rate is 40 kHz. For each pixel 800 intensity values are acquired. In figures 3.9(a) and 3.9(b) the scans in the absence and in the presence of the probe are shown.

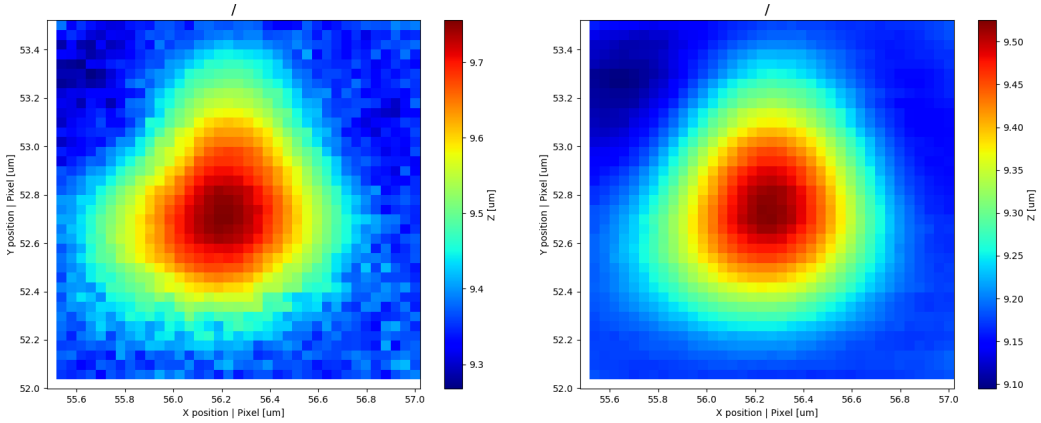

(a) (b)

Figure 3.9: Scan of a cluster of 353 nm silica beads fixed on a coverslip. (a) Scan in the presence of a 300 nm polystyrene bead probe; (b) Scan in the absence of the probe

In figure 3.10 the effect of the subtraction is shown.

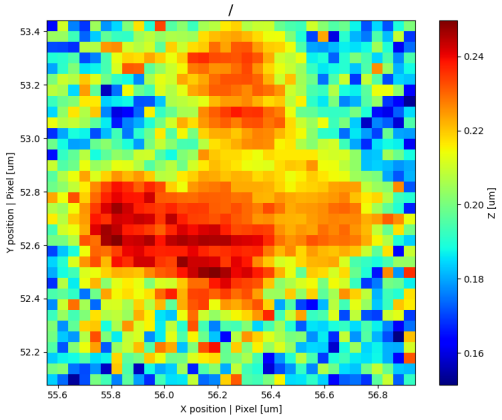

Figure 3.10: Effect of the subtraction between the scan in the presence and in the absence of the probe.

Scan of a known structure

We imaged a known structure, fabricated by lithography by R.Desgarceaux. This is a cylindrical structure, with the diameter of approximately 15 μm and the height of 280 nm. In figure 3.11 an SEM image of this structure is shown.

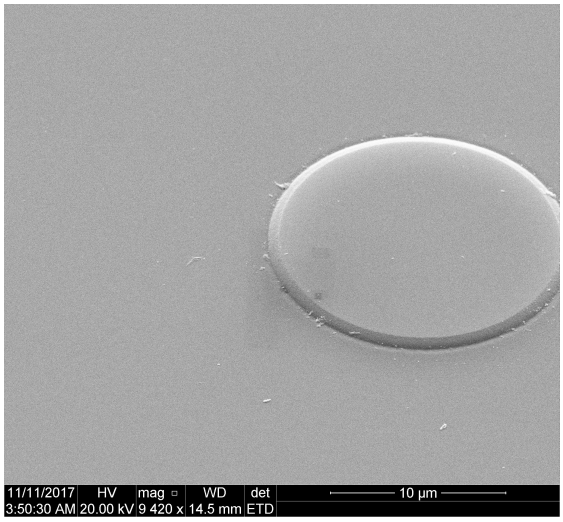

Figure 3.11: SEM image of the scanned structure (image by courtesy of R. Desgarceaux).

The scan of this structure is performed with the cylinder-shaped probe shown in figure 3.4(b). In figure 3.12 a low resolution scan of a part of the structure is shown. The piezoelectric stage is moved by the steps of 500 nm and the acquisition rate is 40 kHz. For each pixel 800 intensity values are acquired.

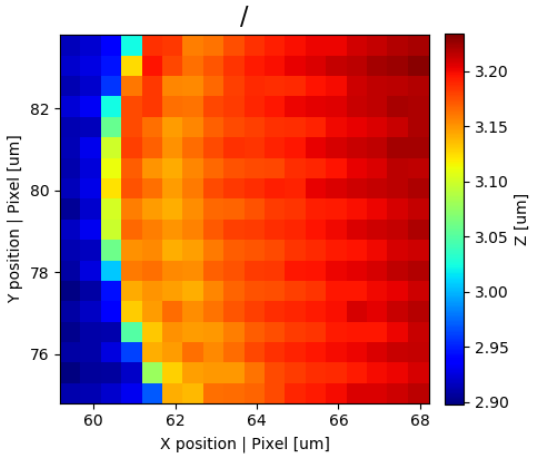

Figure 3.12: Low resolution PFM image of the structure, in the presence of the probe.

Only a small part of this scan is considered for a higher resolution scan. In the figures (3.13(a) and 3.13(b)) the scan in the presence of the cylindrical probe and the scan with the empty trap are shown. The piezoelectric stage is moved by steps of 50 nm and the acquisition rate is 40 kHz. For each pixel 800 intensity values are acquired.

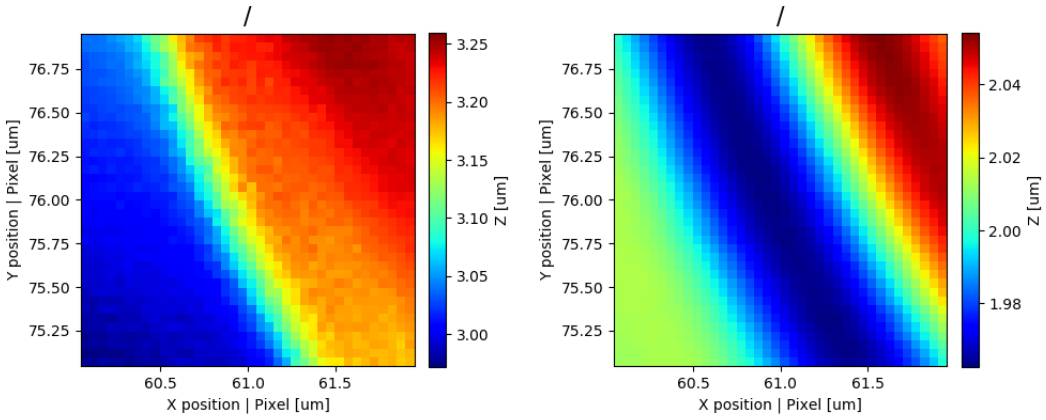

(a) (b)

Figure 3.13: Scan of a part of the structure. (a) Scan in the presence of the cylindrical probe; (b) Scan in the absence of the probe.

The result of the subtraction is shown in figure 3.14.

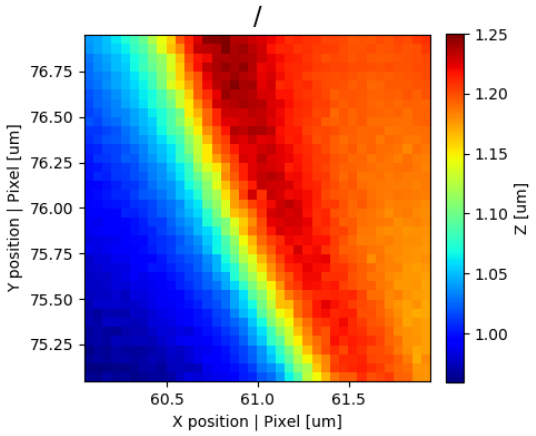

Figure 3.14: Effect of the subtraction between the scan in the presence and in the absence of the probe.

For a better visualization a 3d surface plot and the profile of this difference are shown in figure 3.15 and 3.16.

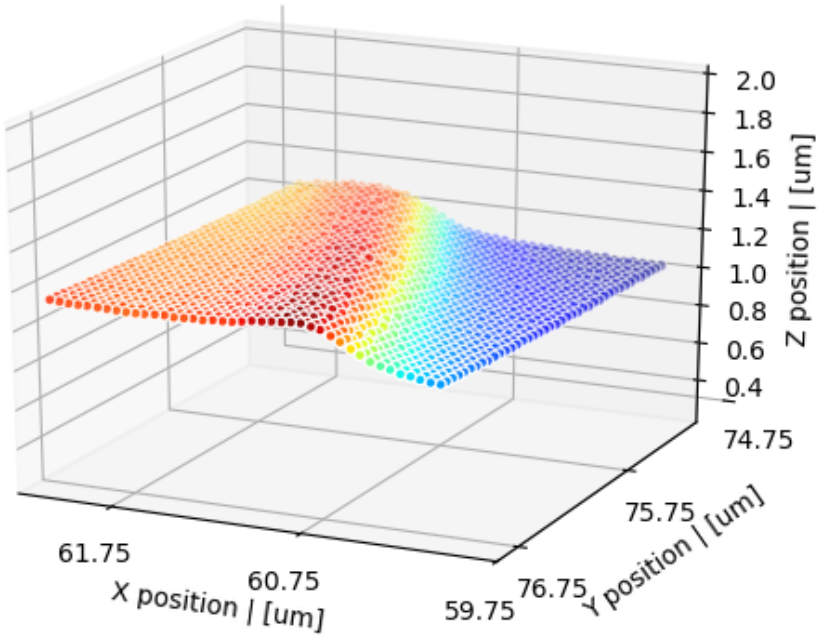

Figure 3.15: Three dimensional visualization of the figure 3.14.

In figure 3.16 the profile of the structure is shown. The three curves are obtained for the last pixel row (y = 77 μm) in the presence and in the absence of the probe and after the subtraction.

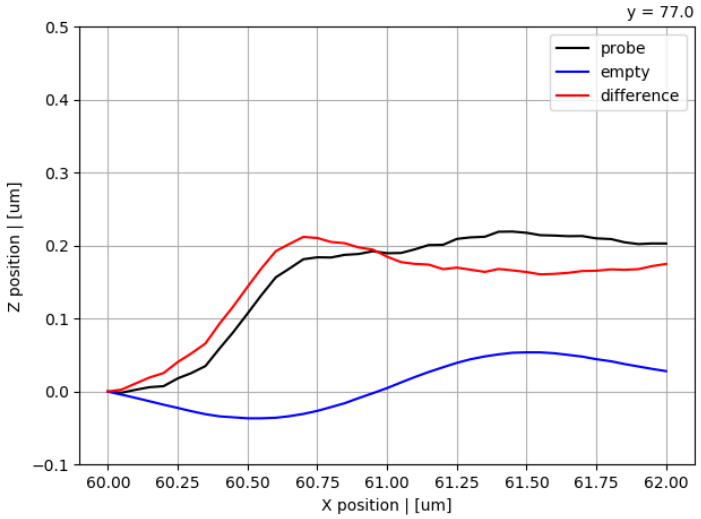

Figure 3.16: Profile of the structure referred to the y = 77 μm position.

Discussion

4.1 Double-beam PFM

Several difficulties were encountered while using this approach. When the two traps are close (around 1 μm) and the probe has a comparable dimension, it happens that the probe is shared between the two traps, moving from one trap to the other, making the completion of a full scan impossible.

This problem is resolved by increasing the distance between the two traps. This way, the scan time increases but, in case of big structures, the time saving is still relevant. In addition, even if the probe stays in only one trap, there could be a crosstalk between the two traps, in particular, if the power in the two beams is higher than 10 mW. This issue is evidenced in figure 3.7(b), where in the squared region the shadow due to the crosstalk is highlighted. We observe that in the image in the absence of the probe there is a dark contour with respect to the background, located exactly in the position of the two beads in the image obtained in the presence of the probe. This means that part of the signal from the first beam is detected in the second beam path.

In addition, in the figure 3.8, we observe that the signal subtraction procedure does not provide additional information. On the contrary it seems to distort the image of the two beads, which we expected to be spherical.

As described in the section 1.3, the idea of the subtraction is based on the assumption that the two traps are identical. This procedure eliminates the scattering due to the empty trap and considers only the signal due to the probe displacement. So, if the two traps of the double-beam PFM are not identical, the subtraction not only does not provide additional information on the scanned structure, but it also brings to misrepresented results. The difference between the two traps can be caused by several factors: a displacement in the axial position of the focus of the trap, a tilt of the focused beam, differences in the diameter of the expanded beams caused by the use of two independent telescopes, or the non equivalent detection part. In conclusion, there are several factors which are not straightforward to control, therefore, we returned to the initial single-beam PFM configuration where both the empty scan and the scan with a probe are performed using a single beam.

However, different ways to build a double beam PFM are present in the literature with

an idea of splitting the two beams not relying on their different polarization. One of the methods is based on time sharing: the two traps, displaced by 2 μm, are formed from the same beam using a beam steering device, based on galvanometric mirrors [33].

4.2 Single-beam PFM

This configuration ensures that the beam used for the scan with a probe and for the empty trap scan is the same, as mentioned previously. The scanning time is longer with respect to the double-beam PFM for bigger structures but is comparable for scanning of small structures with high resolution.

Scan of a cluster of beads

From the figures 3.9(a) and 3.9(b) we observe that the images obtained in the presence and in the absence of the probe evidence a structure of the dimensions around 1 μm by 1 μm. Knowing that the sample was composed from 353 nm silica beads, the guess is that this pattern is due to a small cluster of three or four beads. Neverthless, it is not possible to distinguish how many beads are present in the scanning area. Therefore, the subtraction between these two images is crucial to obtain additional information.
In the figure 3.10 we can clearly see that the scanned pattern was formed by four beads, which are not detectable by considering uniquely the two separates scans. However, we have no information about the actual axial location of these four beads. It seems, in fact, that the central bead in the lower row is located slightly higher than the others. This could be caused by the difference in size with respect to the nominal value or by the placement of this central bead on the top of something else, like the part of the edges of the two neighbouring beads.

From this uncertainty on the real shape of the sample arises the necessity of knowing exactly what we are scanning, in order to evaluate the PFM performance.

Scan of a known structure

The chosen sample is fabricated by lithography by R.Desgarceaux, and its theoretical dimensions are known thanks to the SEM image 3.11.

In figure 3.15, we observe that the effect of the subtraction does not provide more of the structural details, contrary on to what we saw in figure 3.10. This is because there are no narrow details in this structure that can be resolved by the subtraction method.

We can estimate the height of the structure as being approximately 210 nm while the theoretical height is around 280 nm. We see that the lateral face of the structure is characterized by a slope, as expected both from the SEM image (figure 3.11) and from the lithography process, which does not permit the engraving of straight walls. In addition, from the profile shown in figure 3.16 we can see the contribution of the subtraction. The scan in presence of the probe evidences a hump which is mediated by the subtraction. On the contrary, the line referred to the difference seems to indicate the presence of an edge

at the end of the rising slope, which we do not see in the SEM image. An AFM image of this structure will be performed in order to evaluate the accuracy of these measurements.

Conclusions

The aim of this thesis was to understand the physical principles of the optical trapping and the micro-manipulation of the trapped objects, to master the calibration methods of the optical trap and the detection system, to get familiar with the back focal plane interferometry, and based on the obtained theoretical and practical knowledge to use and to improve the technique of the probe scanning microscopy with optical tweezers, the Photonic Force Microscopy.

In the first part of the work, a user-friendly Graphical User Interface was created. It was based on the existing Python scripts that include procedures of the calibration of the optical trap and the sensitivity of the detectors, based on thermal motion and sinusoidally driven motion of the probe in the trap. In addition, several scripts were written for the the sub-pixel cross-correlation and the analysis using the quantiles of the data. They were included to the topographical image reconstruction procedure.

The second part was dedicated to the validation of the two configurations of the PFM, the double-beam and the single-beam. The double-beam PFM was thought to reduce scanning time of the large samples ($\sim$5 μm) and thus the mechanical drift in the measurement by introducing the second "reference" beam to the existing trapping beam at a certain distance. The implementation of the double-beam was based on the splitting of the initial beam into two orthogonal polarizations. This strategy was only applicable for a low intensity beam, since the interference between the two polarizations was not negligible and introduced false topography into the final image. Moreover, the precise spacial alignment of the two traps was extremely complicated. Therefore, this technique was not approved for further development.

The classical single-beam PFM was used to scan over the smaller objects ($\sim$1 μm). The empty trap reference scan and the scan with a probe were performed by the same beam. Therefore, we could verify the reference-probe image subtraction method by Friedrich et al. to distinguish the features with the resolution beyond the diffraction limit.

We tested a variety of cylindrical probes in order to improve the axial resolution compared to that of the the traditional spherical probe. Several cylindrical probe types were tested in order to find the one that guarantees the best acquisition and control over its orientation in the trap. As a result, we propose a method to relate the orientation of the probe in the optical trap (tip upwards or downwards) to the intensity level of the axial signal. In addition, a single preliminary measurement points towards a probable

method to estimate the length of the tip. This observation has to be confirmed on a larger number of probes.

Further experiments and technical development are necessary to assess the performance of this PFM on the known structures and exploring the variety of the probe geometries.

Regardless its high complexity, the PFM stays a potential complementary technique to the other more advanced scanning probe microscopy techniques, especially, it is interesting for the biological applications.

References

[1] A. Ashkin, "Acceleration and trapping of particles by radiation pressure", *Physical review letters*, vol. 24, no. 4, p. 156, 1970.

[2] G. A. Askaryan, "Effect of the field gradient of an intense electromagnetic beam on electrons and atoms", Tech. Rep., Jan. 1991.

[3] A. Ashkin, J. M. Dziedzic, J. Bjorkholm, and S. Chu, "Observation of a single-beam gradient force optical trap for dielectric particles", *Optics letters*, vol. 11, no. 5, pp. 288–290, 1986.

[4] A. Ashkin, J. M. Dziedzic, and T. Yamane, "Optical trapping and manipulation of single cells using infrared laser beams", *Nature*, vol. 330, no. 6150, pp. 769–771, 1987.

[5] A. Ashkin and J. Dziedzic, "Internal cell manipulation using infrared laser traps", *Proceedings of the National Academy of Sciences*, vol. 86, no. 20, pp. 7914–7918, 1989.

[6] S. Chu, "Laser manipulation of atoms and particles", *Science*, pp. 861–866, 1991.

[7] M. H. Anderson, J. R. Ensher, M. R. Matthews, C. E. Wieman, E. A. Cornell, *et al.*, "Observation of bose-einstein condensation in a dilute atomic vapor", *Science*, vol. 269, no. 5221, pp. 198–201, 1995.

[8] A. Ashkin, "History of optical trapping and manipulation of small-neutral particle, atoms, and molecules", *IEEE Journal of Selected Topics in Quantum Electronics*, vol. 6, no. 6, pp. 841–856, 2000.

[9] K. Svoboda, C. F. Schmidt, B. J. Schnapp, and S. M. Block, "Direct observation of kinesin stepping by optical trapping interferometry", *Nature*, vol. 365, no. 6448, p. 721, 1993.

[10] C. Veigel, M. L. Bartoo, D. C. White, J. C. Sparrow, and J. E. Molloy, "The stiffness of rabbit skeletal actomyosin cross-bridges determined with an optical tweezers transducer", *Biophysical journal*, vol. 75, no. 3, pp. 1424–1438, 1998.

[11] C. G. Baumann, S. B. Smith, V. A. Bloomfield, and C. Bustamante, "Ionic effects on the elasticity of single dna molecules", *Proceedings of the National Academy of Sciences*, vol. 94, no. 12, pp. 6185–6190, 1997.

[12] A. Ashkin and J. Dziedzic, "Optical levitation by radiation pressure", *Applied Physics Letters*, vol. 19, no. 8, pp. 283–285, 1971.

[13] E. R. Dufresne and D. G. Grier, "Optical tweezer arrays and optical substrates created with diffractive optics", *Review of scientific instruments*, vol. 69, no. 5, pp. 1974–1977, 1998.

[14] J. E. Curtis, B. A. Koss, and D. G. Grier, "Dynamic holographic optical tweezers", *Optics communications*, vol. 207, no. 1, pp. 169–175, 2002.

[15] D. Burnham and D. McGloin, "Holographic optical trapping of aerosol droplets", *Optics express*, vol. 14, no. 9, pp. 4176–4182, 2006.

[16] S. C. Chapin, V. Germain, and E. R. Dufresne, "Automated trapping, assembly, and sorting with holographic optical tweezers", *Optics express*, vol. 14, no. 26, pp. 13 095–13 100, 2006.

[17] D. G. Grier, "A revolution in optical manipulation", *Nature*, vol. 424, no. 6950, pp. 810–816, 2003.

[18] Y. Roichman and D. G. Grier, "Holographic assembly of quasicrystalline photonic heterostructures", *Optics express*, vol. 13, no. 14, pp. 5434–5439, 2005.

[19] L. Rugani, "Optical traps illuminate the subcellular world", *Biophotonics International*, vol. 13, no. 9, p. 40, 2006.

[20] J. Sleep, D. Wilson, R. Simmons, and W. Gratzer, "Elasticity of the red cell membrane and its relation to hemolytic disorders: An optical tweezers study", *Biophysical journal*, vol. 77, no. 6, pp. 3085–3095, 1999.

[21] Z. Li, B. Anvari, M. Takashima, P. Brecht, J. H. Torres, and W. E. Brownell, "Membrane tether formation from outer hair cells with optical tweezers", *Biophysical journal*, vol. 82, no. 3, pp. 1386–1395, 2002.

[22] R. Nambiar, R. E. McConnell, and M. J. Tyska, "Control of cell membrane tension by myosin-i", *Proceedings of the National Academy of Sciences*, vol. 106, no. 29, pp. 11 972–11 977, 2009.

[23] A. Pralle, E.-L. Florin, E. H. Stelzer, and J. H. Hörber, "Photonic force microscopy: A new tool providing new methods to study membranes at the molecular level", *Single Molecules*, vol. 1, no. 2, pp. 129–133, 2000.

[24] K. C. Neuman and S. M. Block, "Optical trapping", *Review of scientific instruments*, vol. 75, no. 9, pp. 2787–2809, 2004.

[25] A. Ashkin, "Forces of a single-beam gradient laser trap on a dielectric sphere in the ray optics regime", *Biophysical journal*, vol. 61, no. 2, pp. 569–582, 1992.

[26] Y. Harada and T. Asakura, "Radiation forces on a dielectric sphere in the rayleigh scattering regime", *Optics communications*, vol. 124, no. 5-6, pp. 529–541, 1996.

[27] T. A. Nieminen, V. L. Loke, A. B. Stilgoe, G. Knöner, A. M. Brańczyk, N. R. Heckenberg, and H. Rubinsztein-Dunlop, "Optical tweezers computational toolbox", *Journal of Optics A: Pure and Applied Optics*, vol. 9, no. 8, S196, 2007.

[28] J. A. Kas. (2017). Optical forces, [Online]. Available: `http://home.uni-leipzig.de/pwm/web/?section=introduction&page=opticaltraps` (visited on 11/10/2017).

[29] L. P. Ghislain and W. W. Webb, "Scanning-force microscope based on an optical trap", *Optics Letters*, vol. 18, no. 19, pp. 1678–1680, 1993.

[30] E.-L. Florin, J. H. Hörber, and E. H. Stelzer, "High-resolution axial and lateral position sensing using two-photon excitation of fluorophores by a continuous-wave nd: Yag laser", *Applied physics letters*, vol. 69, no. 4, pp. 446–448, 1996.

[31] J. Hörber, "Adapting afm techniques for studies on living cells", *Force Microscopy: Applications in Biology and Medicine*, pp. 137–158, 2006.

[32] C. Tischer, S. Altmann, S. Fisinger, J. H. Hörber, E. H. Stelzer, and E.-L. Florin, "Three-dimensional thermal noise imaging", *Applied Physics Letters*, vol. 79, no. 23, pp. 3878–3880, 2001.

[33] L. Friedrich and A. Rohrbach, "Surface imaging beyond the diffraction limit with optically trapped spheres", *Nature nanotechnology*, vol. 10, no. 12, pp. 1064–1069, 2015.

[34] P. C. Seitz, E. H. Stelzer, and A. Rohrbach, "Interferometric tracking of optically trapped probes behind structured surfaces: A phase correction method", *Applied optics*, vol. 45, no. 28, pp. 7309–7315, 2006.

[35] Z. Santybayeva and F. Pedaci, "Optical torque wrench design and calibration", *Optical Tweezers: Methods and Protocols*, pp. 157–181, 2017.

[36] M. W. Allersma, F. Gittes, R. J. Stewart, C. F. Schmidt, *et al.*, "Two-dimensional tracking of ncd motility by back focal plane interferometry", *Biophysical journal*, vol. 74, no. 2, pp. 1074–1085, 1998.

[37] K. Svoboda and S. M. Block, "Biological applications of optical forces", *Annual review of biophysics and biomolecular structure*, vol. 23, no. 1, pp. 247–285, 1994.

[38] S. F. Tolić-Nørrelykke, E. Schäffer, J. Howard, F. S. Pavone, F. Jülicher, and H. Flyvbjerg, "Calibration of optical tweezers with positional detection in the back focal plane", *Review of scientific instruments*, vol. 77, no. 10, p. 103 101, 2006.

[39] W. Stockwell, "Bias stability measurement: Allan variance", *Crossbow Technology, Inc., Tech. Rep*, 2004.

[40] F. Czerwinski, A. C. Richardson, and L. B. Oddershede, "Quantifying noise in optical tweezers by allan variance", *Optics express*, vol. 17, no. 15, pp. 13 255–13 269, 2009.

[41] A. Rohrbach, C. Tischer, D. Neumayer, E.-L. Florin, and E. H. Stelzer, "Trapping and tracking a local probe with a photonic force microscope", *Review of Scientific Instruments*, vol. 75, no. 6, pp. 2197–2210, 2004.